NASA/TM–2018–220213

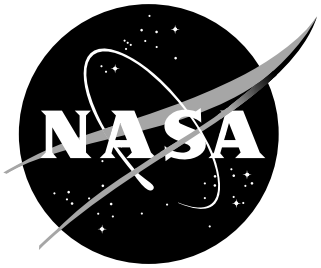

Molecular dynamics of ULTEM 9085 for 3D manufacturing: spectra, thermodynamic properties, and shear viscosity.

Dmitry G. Luchinsky
SGT Inc., Ames Research Center, Moffett Field, California

Halina Hafiychuk
SGT Inc., Ames Research Center, Moffett Field, California

Vasyl Hafiychuk
SGT Inc., Ames Research Center, Moffett Field, California

Kevin R. Wheeler
Ames Research Center, Moffett Field, California

December 2018

NASA STI Program . . . in Profile

Since its founding, NASA has been dedicated to the advancement of aeronautics and space science. The NASA scientific and technical information (STI) program plays a key part in helping NASA maintain this important role.

The NASA STI Program operates under the auspices of the Agency Chief Information Officer. It collects, organizes, provides for archiving, and disseminates NASA's STI. The NASA STI Program provides access to the NASA Aeronautics and Space Database and its public interface, the NASA Technical Report Server, thus providing one of the largest collection of aeronautical and space science STI in the world. Results are published in both non-NASA channels and by NASA in the NASA STI Report Series, which includes the following report types:

- TECHNICAL PUBLICATION. Reports of completed research or a major significant phase of research that present the results of NASA programs and include extensive data or theoretical analysis. Includes compilations of significant scientific and technical data and information deemed to be of continuing reference value. NASA counterpart of peer-reviewed formal professional papers, but having less stringent limitations on manuscript length and extent of graphic presentations.
- TECHNICAL MEMORANDUM. Scientific and technical findings that are preliminary or of specialized interest, e.g., quick release reports, working papers, and bibliographies that contain minimal annotation. Does not contain extensive analysis.
- CONTRACTOR REPORT. Scientific and technical findings by NASA-sponsored contractors and grantees.
- CONFERENCE PUBLICATION. Collected papers from scientific and technical conferences, symposia, seminars, or other meetings sponsored or co-sponsored by NASA.
- SPECIAL PUBLICATION. Scientific, technical, or historical information from NASA programs, projects, and missions, often concerned with subjects having substantial public interest.
- TECHNICAL TRANSLATION. English- language translations of foreign scientific and technical material pertinent to NASA's mission.

Specialized services also include creating custom thesauri, building customized databases, and organizing and publishing research results.

For more information about the NASA STI Program, see the following:

- Access the NASA STI program home page at ***http://www.sti.nasa.gov***
- E-mail your question via the Internet to help@sti.nasa.gov
- Fax your question to the NASA STI Help Desk at 443-757-5803
- Phone the NASA STI Help Desk at 443-757-5802
- Write to:
  NASA STI Help Desk
  NASA Center for AeroSpace Information
  7115 Standard Drive
  Hanover, MD 21076–1320

NASA/TM–2018–220213

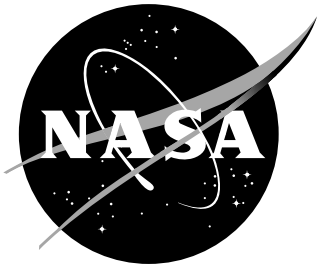

Molecular dynamics of ULTEM 9085 for 3D manufacturing: spectra, thermodynamic properties, and shear viscosity.

Dmitry G. Luchinsky
SGT Inc., Ames Research Center, Moffett Field, California

Halina Hafiychuk
SGT Inc., Ames Research Center, Moffett Field, California

Vasyl Hafiychuk
SGT Inc., Ames Research Center, Moffett Field, California

Kevin R. Wheeler
Ames Research Center, Moffett Field, California

National Aeronautics and
Space Administration

Ames Research Center
Moffett Field, California 94035-2199

December 2018

Acknowledgments

We thank Gabriel Jost for the help in setting up, profiling, and running simulations on Amazon Web Services. We are grateful to Taku Ozawa, Hiroya Nitta and Kenta Chaki for providing J-OCTA software, support and valuable discussion. We thank Tracie Prayer for providing experimental data and guidance.

Available from:

NASA Center for AeroSpace Information
7115 Standard Drive
Hanover, MD 21076-1320
443-757-5802

Abstract

We present results of a molecular dynamic analysis of welding at the polymer-polymer interface. The analysis is performed for polyetherimide/polycarbonate polymer blends. The work is motivated by the applications to 3D manufacturing in space. In the first part of the report, we discuss bulk and spectral characteristics of the amorphous polymer blends. The vibrational and infra-red spectra obtained using auto-correlation functions calculations in molecular dynamics are compared with the experimental spectra. The mechanical and thermal properties of the samples including heat capacity, bulk modulus, and thermal expansion coefficients are estimated and compared with experimental values. In the second part of the report, we discuss the result of molecular dynamical modeling of shear viscosity in a fully atomistic model of amorphous polymer blends with flat interface. The key result of the research is the demonstration of shear thinning behavior of the shear viscosity as a function of shear rate which is in good agreement with experimental data.

Introduction

Controlling properties of matter on atomic scale is one the main goals of modern nanotechnology [1] that has multiple applications in aerospace including e.g. thermal protection materials [2], 3D manufacturing [3], ice-phobic and water resistant coatings [4], nanomedicine [5], biosensing [6], rechargeable batteries [7], and water treatment [8] to mention a few.

At present, Molecular Dynamics (MD) modeling of polymers has advanced to the point where predictions can be used to guide experiments [9] and/or to provide useful insight into the structure property relation of polymer materials. In particular, the MD modeling was successfully applied to analyze properties of polyetherimides [3, 10–14].

Much less is known about structure property relation at atomistic level for polyetherimide (PEI) polycarbonate (PC) blends. These blends are high performance amorphous thermoplastics with good thermal stability and remarkable modulus of elasticity and tensile strength [15]. They are widely used in aerospace applications and, in particular, for 3D manufacturing in space. Understanding their structure-process-property balance is of significant importance for the applications [16]. However, atomistically informed insight into molecular dynamics of these structures remains limited. For example, Zhang and co-authors [17] published one of the first research on MD analysis of miscibility and anomalous exhibit of two distinct glass transition temperatures in PEI/PC blends. The interfacial interaction between ULTEM and a variety of low molecular weight liquids have been evaluated using molecular dynamic

simulations in [9].

Our primary interest in this work is understanding the relation between reptation of the polymer chains at the interface and the resulting strength of the 3D manufactured structure. During additive manufacturing, two pieces of polymer melts are brought together above glass transition temperature and allowed to inter-diffuse. The recovery of the bulk strength occurs due to entanglement of the polymer chains at the interface and is assumed to be proportional to the mass exchange between the two polymer pieces. The temperature regime and the time scale of this motion and their dependence on the polymer structure are key parameters of interest for applications.

The molecular dynamics of such motion was mainly analyzed using coarse-grained bed-spring models [18–21]. These insightful simulations do not take into account the flexibility and electrostatic properties of the polymer chains. The latter, however, are known to significantly influence the physics of the interface welding [3, 22] as well as the structure of the polymer chains [23].

The polymer welding at the interface is of particular interest in additive manufacturing (AM), which is gaining increasing importance in industry for both prototyping and production of functional parts [24]. The global market for AM products and services has grown into a $1.3 billion industry, and it is estimated to grow to over $5 billion by 2020 [24].

According to [25] Stratsys offers three choices as high performance filaments: Ultem 1000, Ultem 9085 and Polyphenylsulfone (PPSF). Both the Ultem grades are based on polyetherimide (PEI) and they are certified for use in the automotive, medical and aerospace fields. Ultem 1000 is a pure PEI, while Ultem 9085 is reported to be a mixture of PEI and polycarbonate copolymer blend incorporated for improved flow [26].

The mechanical properties of welded interface of materials such as Ultem 9085 is at the focus of the present report.

Zaldivar et al. [26] showed recently that Ultem 9085 printed specimen mechanical properties are significantly affected by build orientation. The strength utilization in terms of FDM/injection molded performance can vary from 85.8% for edge printed specimens to 46.5% for up printed samples. This means that the final properties of the FDM printed part are highly anisotropic. The lower performances, compared to injection molded specimens, were the result of the voids in FDM printed parts between fused filaments. Motaparti et al. [27] recently showed that the strength of a thermoplastic interface within FDM part is directly proportional to the intermolecular diffusion across the interface between the fused filaments. The relevance of bond quality between adjacent filaments depends on printing parameters, but, also, on the melt viscosity of the polymer used for the filaments. However, to the best of our knowledge, this aspect has been investigated in the literature by only a few studies from McIlroy et al. [**?**, 28].

To address these issues we develop a fully atomistic model of the polymer-polymer interface in PEI/PC blends. We analyze spectral and thermodynamic properties of the MD samples to estimate the shear viscosity as a function of temperature and welding time. To validate the predictions based on molecular dynamic simulations we use two sets of experimental data. The first set was provided by the MSFC group and includes infrared absorbance spectra and specific heat capacity for ULTEM 9085. The second set of data was provided by Prospector LLC and includes results of the following properties measured for ULTEM 1000 [29]: (i) density; (ii) bulk modulus ; (iii) coefficient of linear thermal expansion; (iv) specific heat capacity (with (i) to (iv) measured as functions of temperature); (v) viscosity as a function of shear rate; and (iv) stress as a function of strain.

The overall goal of the project can be formulated as follows. Develop fully atomistic model of polymer-polymer interface capable of reproducing experimental data for amorphous blends of polyetherimide and polycarbonate. Validate model by comparison molecular dynamics predictions with a large set of experimental data. Use the validated model to estimate strain stress curves, shear viscosity as a function of shear rate, and relaxation time at the polymer-polymer interface. Apply estimated parameters to the strength model of the manufactured parts developed in our group.

This report is organized as follows. After providing some details of modeling in Sec. 1 and Sec. 2 we discuss spectral properties of the samples. Next, we analyze thermodynamic and mechanical properties of the amorphous PEI/PC melts and compare results of MD modeling with experimental data in Sec. 4. Some additional details of modeling polymer-polymer interface are given in Sec. 5. The estimations of the shear viscosity is discussed in Sec. 6. The application of the obtained results to the analysis of the strength of the manufactured parts is discussed in Sec. s:application. Finally, the conclusions are drawn and the future work is outlined in Sec. “Conclusions”.

1 Building amorphous cell of PEI/PC blends

The standard way of preparing polymer blends for MD simulations is to create an amorphous cell [9, 17][1]. In this work, we also followed this approach. The amorphous cells of ULTEM 9085 are blends of PEI and PC. PEI based blends can be mixed in a batch mixer (Brabender 50 EHT,

[1] According to the basic definitions amorphous cells can be described as follows: Think of how spaghetti noodles look on a plate. These are similar to how linear polymers can be arranged if they lack specific order, or are amorphous. Controlling the polymerization process and quenching molten polymers can result in amorphous organization. An amorphous arrangement of molecules has no long-range order or form in which the polymer chains arrange themselves.

Brabender & Co., Duisburg, Germany) controlled by a Lab-Station. The content of PC in the blends may vary from 0 wt % to 40 wt %. In our studies the content of PC was always close to 20 wt %.

In this section, we describe the process of building and equilibrating of an amorphous cell of polycarbonate/polyetherimide blends. The process of development of the molecular dynamical model of the amorphous cells of PEI/PC blends includes the following steps:

- build repeating unit of each polymer;
- build polymer chain of PEI and PC;
- create cell with randomly placed polymers (amorphous cell);
- equilibrate cell at a given temperature and pressure;

We now describe these steps in more detail.

1.1 Building fully atomistic polymer chain

The chemical structure and the MD representation of the repeating units of the PEI and PC are shown in Fig. 1 and 2.

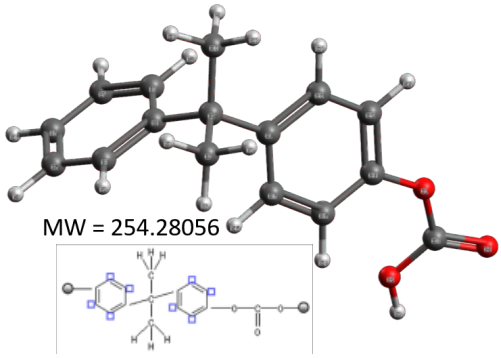

Figure 1: Atomic structure of a single repeated unit (monomer) of polycarbonate (top) with j-octa original structure (bottom) and molecular weight (MW).

The PEI monomer consists of 71 atoms, with molecular weight 628.6269 g/mol. The PC monomer consists of 35 atoms, with molecular weight 256.288 g/mol. The functional groups and their contribution to the cohesive energy are shown in Table 1. An extensive lists of mechanical and thermal properties of polyetherimide and polycarbonate were calculated using the functional group method under an assumption of infinite degree of polymerization. These are provided in the excel file attached to this document.

The results of the molecular dynamic simulations strongly depend on the force field used in calculations. In this work, we use Dreiding force field [30] and OPLS-AA force field . The parameters of this force field are shown in the Appendix. The choice of Dreiding force field

was justified by the fact that it was extensively and successfully used in earlier research on polyimides and it covers all types of interactions in our case. The OPLS-AA force field with quantum corrections was chosen as a result of the best fit to the experimental IR spectra.

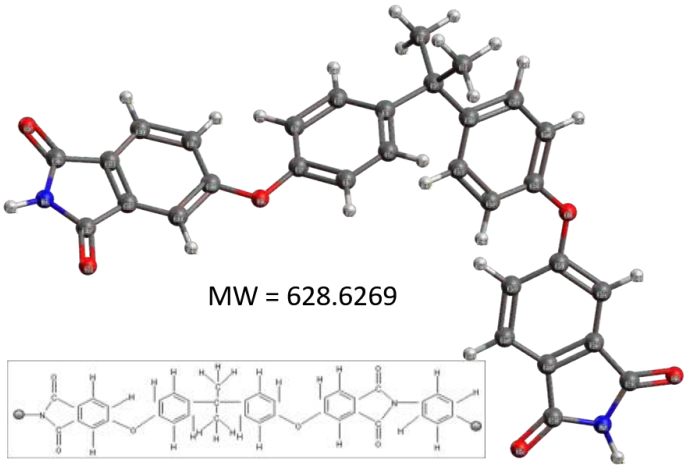

Figure 2: Atomic structure of a single repeated unit (monomer) of polyetherimide (top) with j-octa original structure (bottom) and molecular weight (MW).

Table 1: Functional groups and their contribution to the molar volume and cohesive energy of polyetherimide and polycarbonate.

Group Contribution method	Molar volume [cm^3/mol]	Cohesive energy [J/mol]
Polyetherimide		
-CO-	10.8	17370
_CH3	33.5	4710
>C<	-19.2	1470
-N<	-9	4190
-O-	3.8	3350
Phenylene(p)	52.4	31940
Phenyl(trisubstituted)-2	33.4	31940
Polycarbonate		
0	33.5	4710
>C<	-19.2	1470
Phenylene(p)	52.4	31940
_CO4-(carbonate)	22	17580

The flexibility of the PEI and PC polymers are mainly determined by the flexibility of torsional angles between relatively rigid planes of aromatic rings of the Phthalimide and Bisphenol A fragments. It is the fluctuation of torsional angles defined for these virtual bonds that determine the flexibility and persistence length of polyetherimide chains.

1.2 Quantum corrections

??Quantum corrections to the force field were obtained in J-OCTA [31] by calculating equilibrium distributions of the atom locations in a monomer

unit using quantum chemistry package GAMESS [32,33]. Next, the distributions obtained with classical MD were fitted to quantum mechanical distributions by adjusting coefficients in the classical force field.

We used this approach to obtain quantum corrections to the OPLS-AA and DREIDING force fields. Only OPLS-AA force fields were used in further research due to time limitations.

1.3 Amorphous cell

We prepare two polymer cells with a nearly atomistically flat interface. Initially, the polymer chains were placed at random into the cell with z-size (≈ 70 Å determined by the chain length) and (x, y) cross-section size ($\approx 35 \times 35$ Å) defined by the sample density ($\approx 1 g/cm^3$).

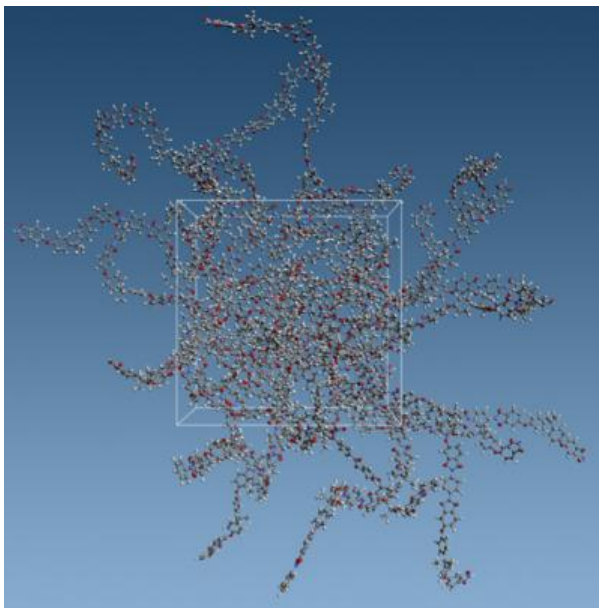

Figure 3: Atomistic models of amorphous cells with PEI/PC polymers blends: Each polymer had 5 repeating monomer units. PEI unit has 70 atoms PC unit has 35 atoms. Cell contains 8 PEI and 4 PC polymers.

The surface of each sample was prepared by moving polymer chains inside the cell at a given interface and using non-periodic reflective boundary conditions BC in Z-direction with Lennard-Johns-wall (LJ-wall) at the interface that was restricting chains motion at the interface during the preparation. The parameters of the LJ-wall at the interface were: (i) cut-off ~10 Å; (ii) sigma ~5 Å; (iii) epsilon ~10 kJ/mol; and (iv) density ~20 g/cm^3.

Both cells were relaxed following the procedure provided in J-OCTA ($T_0 = 600$ K and $P_0 = 1$ atm)

nve_equil_in.in We use NVE equilibration at a given temperature, e.g. T_0;

compress.in The equilibration is followed by compression in the NPT Andersen-Nose-Hoover thermostat at T_0 and $P = 100$ MPa;

nve_equil_after_compress_in.in The compression is followed by equilibration in the NVE equilibration at T_0;

equil_in.in

nvt_equil_in.in The equilibration is followed by relaxation in the NPT Andersen-Nose-Hoover thermostat at T_0 and P_0;

nvt_eliminate_trans_in.in Finally, the translational component of the velocity is eliminated in the NVT Nose-Hoover thermostat at T_0 and zero pressure.

Each step was computed during 50 ps with time step 1 fs. The resulting amorphous cells are discussed in more details in Sec. 5.

In addition, a small cell (5,166 atoms) was built without interface for fast prototyping of measurements, see figure 3.

2 Important considerations

It is important to recognize the requirements of the size of the cell and the corresponding computing capabilities. First of all, we should emphasize that the simulations of the polymer - polymer interface are the most demanding simulations both in terms of the size and required computing power. The key parameters that influence the desired computational time are the following:

- the size of the cell has to be approximately a few lengths of the polymer chain;
- the length of the polymer chain (i.e. the degree of polymerization of ultem) in real polymers is usually about 70 lengths of a repeating unit;
- 5 PEI units span approximately 100 Å distance;
- 100x100x100 Å cell unit with density $1.2 g/cm^3$ of PEI/PC blend will have approximately 90,000 atoms

To estimate computer time required for simulations of PEI/PC blends we performed extensive profiling of the LAMMPS [34,35] computer capabilities on ARC NAS supercomputer. It has to be emphasized that the cell size with 90,000 atoms could not be simulated with our current computing capabilities. The maximum cell size for fully atomistic simulations with LAMMPS was $\leq$ 20,000.

The results of this profiling for the cell size 44x44x44 Å with 6,888 atoms are shown in the Fig. 4. Note that 24 ns/per day is the minimum productivity required to complete simulations approximately within 2

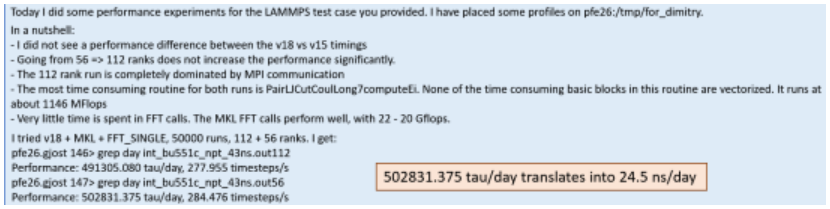

Figure 4: Results of profiling in a nutshell

months. It can be concluded that with our present computing capabilities the maximum cell size that can be used in LAMMPS simulations is around 50x50x50 Å.

Within this project we used small model (which contains 28 polymer chains including 8 PC and 16 PEI chains with 5 repeating monomer units each and total 6,888 atoms) to quickly prototype required simulations of polymer cells with LAMMPS [34, 35] and GROMACS [36–40]. In what follows, we refer to this model as the small system.

However, this cell size is insufficient to grasp the properties of the polymer blends especially in the presence of the interface. Note that to compare thermodynamic properties of amorphous polymer cells with the experiment, even without interface, the required sample size has to be in the range 20,000 to 60,000 atoms as was estimated in [41].

We therefore developed additional MD simulations of a large cell (140x60x60 Å with 41,328 atoms) using molecular dynamics package GROMACS. The simulations of the large system using GROMACS relied on GPU acceleration. The latter turned out to be crucial for completing the project. GROMACS and LAMMPS simulations were used to optimize the performance for specific measurements. In particular, to resolve time dependence of the shear viscosity,l accurate measurements for large shear rates were performed using LAMMPS, while to narrow the gap between MD simulations and experimental data at low shear rates we used GROMACS.

3 Spectral properties

Experimentally observed absorbance spectra of ULTEM 9085 are shown in Fig. 5. Since ULTEM 9085 is a mixture of polyetherimide and polycarbonate the transmittance spectra of polyetherimide and absorbance spectra of polycarbonate are also shown in the inset of the figure.

We now verify that the IR spectra of the ULTEM 9085 can be presented as a weighted mixture of polycarbonate and polyetherimide spectra. To do so, we calculate a blended absorbance spectrum that consists of 80% contribution of the polyetherimide and 20% contribution of polycarbonate. The resulting spectrum is shown in Fig. 7 in comparison with the experimental spectra of ULTEM 9085.

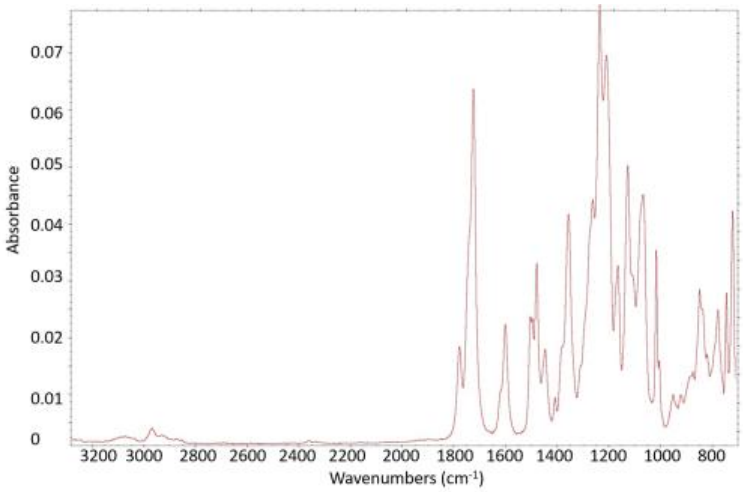

Figure 5: Experimental FTIR spectra of ULTEM 9085 provided by MSFC.

It can be seen from the comparison that there is a very good agreement between blended spectrum and the experimental one. This result confirms the spectral properties of ULTEM 9085 are mainly determined by the properties of two main components PEI and PC. We were not able to clearly identify presence of any other component in the blend.

To get further insight into the spectral properties of ULTEM 9085, we performed functional group analysis of the experimental IR spectra.

3.1 Functional groups

The results of the functional group analysis of the IR spectra of ULTEM are shown in Fig. 8 (left). The analysis reveals contributions due to $C-H$ bonds present in both polymers, see Fig. 8(bottom). Also there is a strong contribution from double $C=O$, double $C=C$, and single $C-O$ bonds present in both polymers, cf Fig. 8 (bottom).

The single $C-N$ bond is only present in polyetherimide, see Fig. 8(bottom), and could be potentially used to determine relative contribution of the PEI to the spectral properties of the sample.

3.2 Quantum chemistry calculations of FTIR spectra

The difference in the spectral properties of PEI and PC components can be further revealed using quantum chemistry calculations. The results of such calculations are shown in Fig. 9. The accuracy of predictions based on quantum chemistry calculations depends on the level of the theory and the basis set.

ab initio methods of quantum chemistry include: the Hartree-Fock (HF) self-consistent-field (SCF) method [42], second-order Møller-Plesset

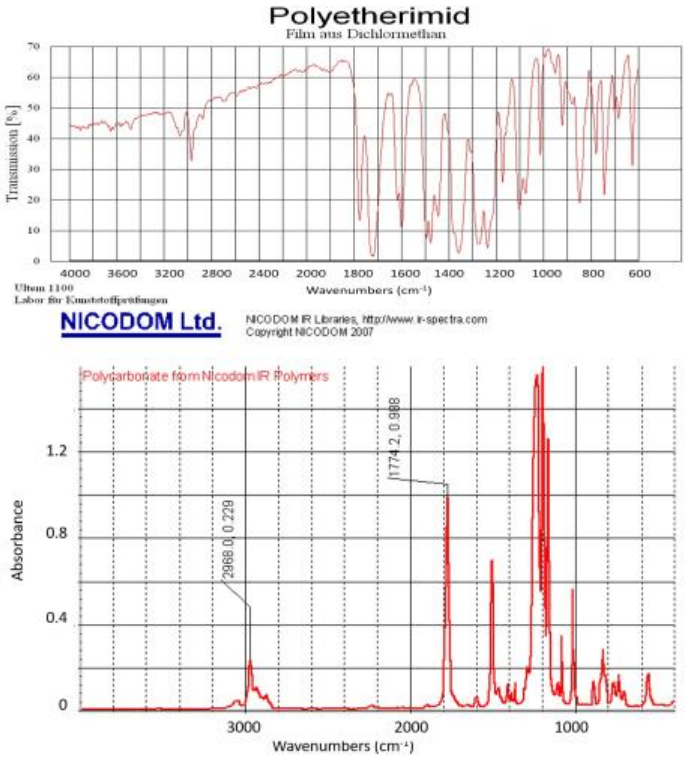

Figure 6: FTIR of polyetherimide (top) reprinted from [**?**] and polycarbonate (bottom) reprinted from http://www.infrared-spectra.com/ with permission.

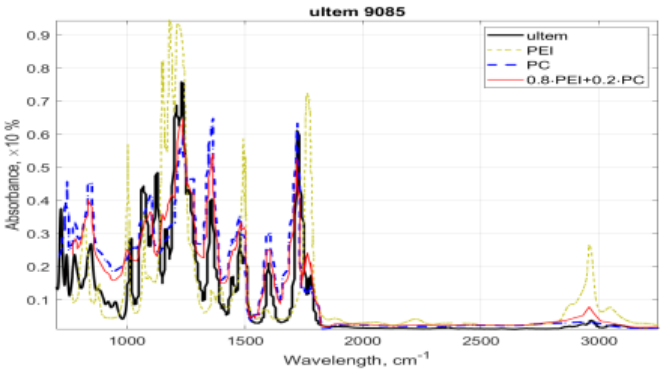

Figure 7: Comparison ot the experimental FTIR spectra of ULTEM 9085 (black solid line)with the individual FTIR spectra measured for PEI (blue dotted line), PC (green dotted line), and the sum of PEI and PC spectra calculated in MATLAB (red line).

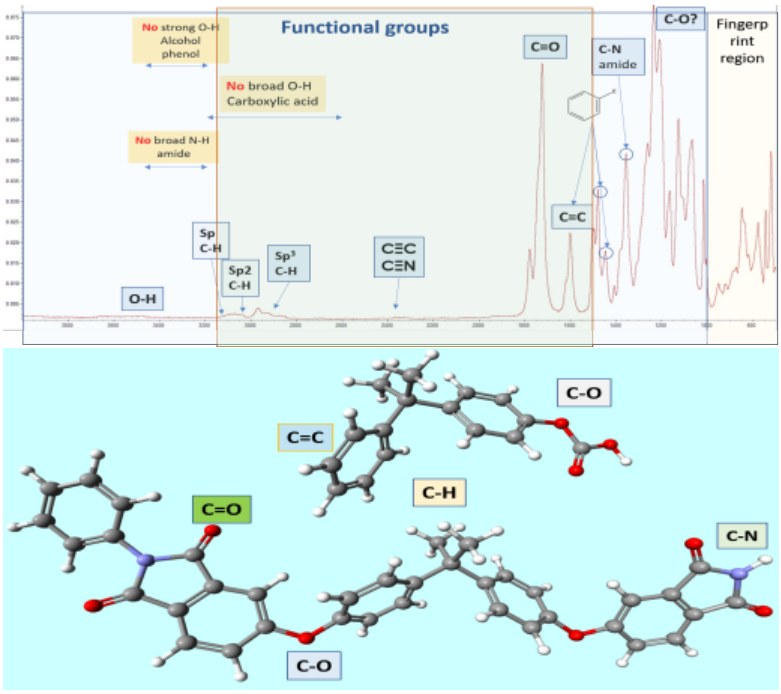

Figure 8: (left)Functional groups corresponding to the main lines observed in absorption spectra. (bottom) Molecular view of the functional groups corresponding to the main lines observed in absorption spectra. Atom codding is: C (gray), O (red), H (white), and N (blue)

perturbation theory (MP2) [43], coupled cluster theory with single and double excitations (CCSD) [44], and CCSD augmented by a perturbational estimate of the effects of connected triple excitations [CCSD(T)] [45]. For N basis functions, the formal cost of these approaches in-

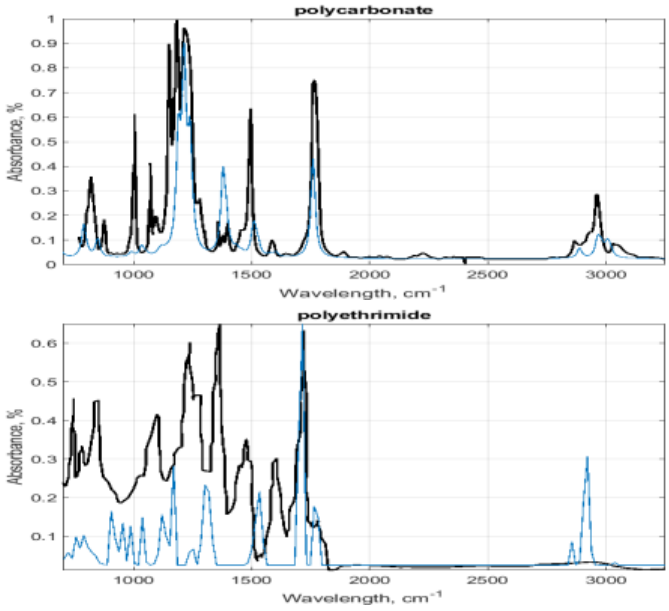

Figure 9: (left) Comparison between experimental spectra of polycarbonate and spectra of a single unit of PC calculated using quantum chemistry package NewChem that applies MøllerPlesset MP2 optimization using 6-31G(d) basis set. (bottom) Comparison between experimental spectra of polyetherimide and spectra of a single unit of PEI calculated using quantum chemistry package and semi-empirical PM3 method in SCIGRESS.

creases as N^4, N^5, N^6, and N^7, respectively, but the accuracy of the results also improves significantly along this series.

In this work, the monomer units are quite large (35 and 70 atoms). Consequently, the number of basis functions is large and the calculations at high theory levels are very expensive. Therefore, the research was limited by the semi-empirical methods and MP2 level of the theory with 6-31G basis set (see John Pople classification of the basis sets [46]). Accordingly, the results shown in the Fig. 9 have limited accuracy and only allow for semi-quantitative comparison with the experiment. However, some key features can be quite well reproduced at this level of the theory. For example, the key structure of the peaks at ~ 3000 cm^{-1}, ~ 1800 cm^{-1}, and ~ 1200 cm^{-1} can be seen in IR spectra of polycarbonate calculated with MP2 level of the theory.

3.3 Vibrational and IR spectra of ULTEM 9085

Another method calculating the IR spectra is based on MD simulations. It involves calculations of the mass weighted autocorrelation velocity functions for each type of atoms and an autocorrelation function for the total dipole momentum of the system. In this method, the MD sim-

ulations are recorded with 1-2 ps resolution during 100-500 ps using LAMMPS or GROMACS.

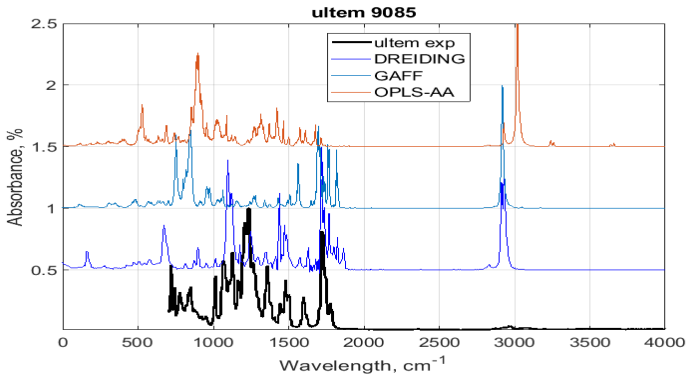

Figure 10: Infrared spectra of amorphous polymer blends obtained using dipole autocorrelation function and three different force fields calculated in MD simulations (three top lines) as compared to the experimental spectra of ULTEM 9085 (bottom line).

The accuracy of these simulations is largely determined by the force field approximation. The three types of the force field were chosen for initial analysis: (i) DREIDING; (ii) GAFF (generalized atomic force field); and (iii) OPLS-AA (Optimized Potentials for Liquid Simulations All-Atom).

The calculated spectra for these three force fields are compared with experimentally measured IR spectra in Fig. 10. It can be noticed that indeed the results strongly depend on the force field and that DREIDING and GAFF force fields provide better agreement with the experiment.

We note, however, that the results of measurements shown in the figure were obtained for the force fields without quantum corrections, see Sec. 1.2. The latter corrections can substantially improve the comparison with the experiment as will be shown in Sec. 4.7

4 Thermodynamic properties

To extend validation of our approach to modeling polymer-polymer interfaces we performed molecular dynamics estimations of the key experimentally measured properties of ULTEM.
In this section we consider MD estimations of the following properties: (i) glass transition temperature T_g; (ii) density of states $S(v)$; (iii) bulk modulus B; (iv) coefficient of thermal expansion α_P; and (v) specific heat capacity c_p.

4.1 Density as a function of temperature

Density of the large sample calculated as a function of the temperature in MD simulations is compared to experimental data for ULTEM 1000 [29] in Fig. 11

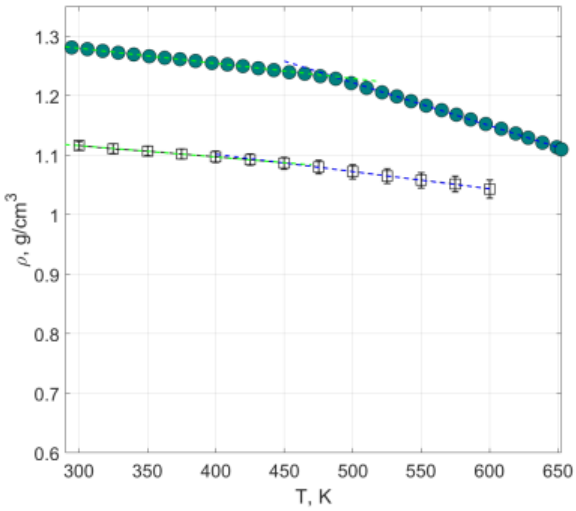

Figure 11: Density of the sample calculated using MD simulations (open squares) as compared to the experimental data (teal circles) obtained for ULTEM 1000 [29]

It can be seen from the figure that the density estimated in the MD simulations is slightly lower than the one obtained in experiment. It can also be noticed that the change in the stop of the density as a function of temperature is more pronounced in the experimental data than in molecular dynamical simulations. Both features are expected on the ground of the common knowledge [41] of the fact that MD slightly underestimate both sample density and effect of the glass transition. Overall, we consider the agreement between MD predictions and experimental data for the density as acceptable. It is possible in principle to compress sample even further by applying very high pressure for extended period of time. But this time consuming exercise is not expected to change substantially obtained results. We now proceed to the estimations of the glass transition temperature in our samples.

4.2 Estimation of the T_g in pure PEI and PC samples

Glass transition temperatures were evaluated by performing NPT simulations while cooling the system at a rate of 20-25 K per 1 ns. The volume at each temperature was computed by averaging results from over 100 last steps dynamic simulations. Volume-temperature responses

were constructed and linear functions were fit to the low and high temperature ranges.

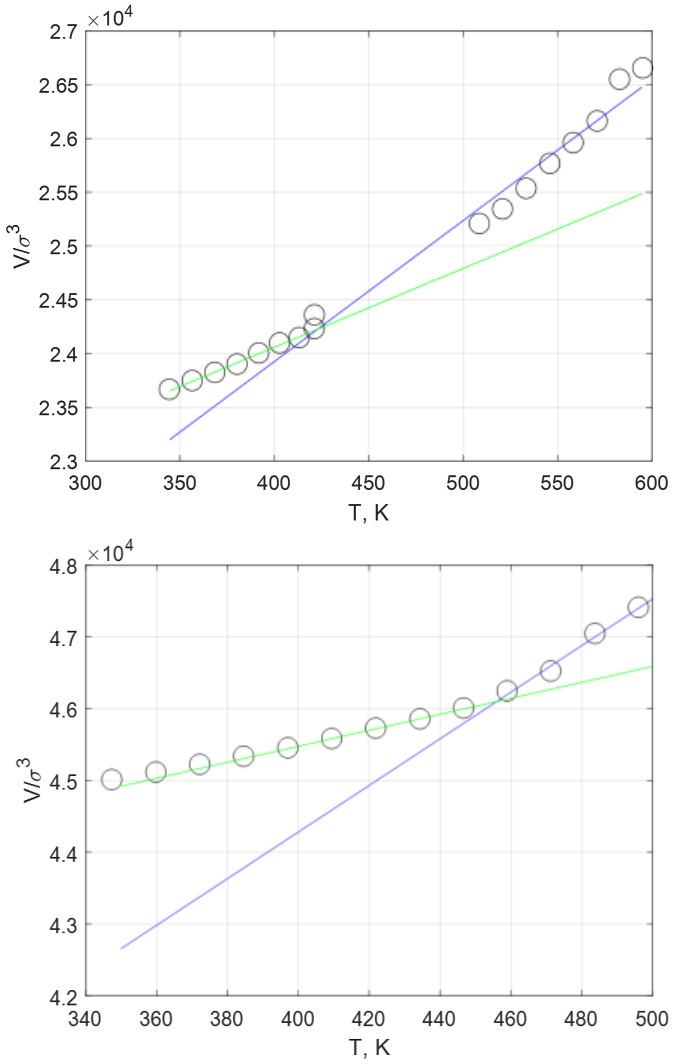

Figure 12: Glass transition temperature estimates based on MD simulations for PC (left) and PEI (bottom).

Free volume theory was first proposed by Fox and Flory [47] to explain the glass transition. The term free volume is used to describe the total volume occupied by the holes. As the temperature increases, the change in free volume or vacant volume of a polymer is small below the glass transition temperature (T_g), but the rate of change increases abruptly at T_g. In fact, measuring the change in the slope of the curve plotting free volume as a function of temperature is one method of obtaining T_g.

The MD estimation of the glass transition temperature for amorphous cell of polycarbonate gives value $T_g \approx 425\ K$, which is in good

agreement with the expected value 420 K. The MD estimation of $T_g \approx$ 457 K for polyetherimide is substantially lower expected value 490 K. The main reasons could be: (i) low degree of polymerization; and (ii) insufficient relaxation time. Note also that Dreiding force tends to underestimate sample density, which may also contribute to underestimation of T_g.

However, different data for T_g of ULTEM 1000 are also available online can be as low as 450 K, see Fig. 13 (bottom). These data are in a better agreement with our estimations and with experimental data for ULTEM 9085 provided by MSFC, which gives for T_g value ~ 178 C (~ 450 K), see Fig. A.1 (bottom).

4.3 Estimation of the T_g in PEI/PC lends

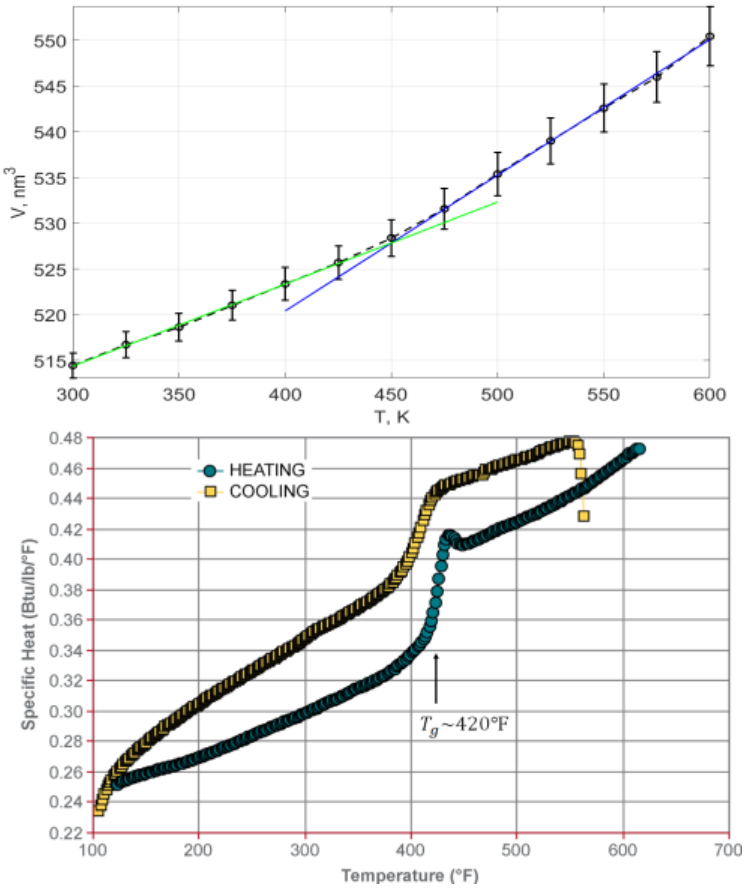

Figure 13: (top) Glass transition temperature calculations based on MD simulations for ULTEM 9085 using LAMMPS. (bottom) Experimental data for heat capacity measurements for ULTEM 1000 [29].

We also performed MD calculations of the glass transition temper-

ature for ULTEM 9085 using the amorphous cell shown in Fig. 3. The results of these calculations based on linear interpolation of the specific volume as a function of temperature are shown in Fig. A.1 (bottom). This estimation suggests a value for $T_g \sim 450$ K, which is in good agreement with both experimental values and MD values obtained for polyetherimide.

We now proceed to the estimations of the bulk modulus.

4.4 Bulk modulus, coefficient of thermal expansion, and heat capacity: background

Bulk modulus, coefficient of thermal expansion, and heat capacity are fundamental material properties and their prediction is important to modeling polymer melts. In addition, theoretical explanation of the jump in the value of these variables at the glass transition remains unsolved and a controversial issue [48, 49]. Therefore, accurate simulations of these properties at glass transition is important both from the point of view of fundamental theory and applications in material science.

There are three main methods of estimation of the cirresponding values from the results of MD simulations: (i) using fluctuations [50, 51]; (ii) using derivatives of the total energy and enthalpy [50, 51]; and (iii) in addition, calculation of tge heat capacity may involve estimation of the density of states [41, 52]. Because these methods provide complimentary information it is instructive to compare estimations obtained by each method.

(i) Fluctuations. Using fluctuations, the following expressions can be obtained [50, 51]. The constant pressure heat capacity is proportional to the variation of enthalpy

$$c_p = \frac{1}{k_B V T^2} \left\langle \sigma_H^2 \right\rangle. \tag{1}$$

The isothermal compressibility is proportional to the variance of volume

$$\beta = \frac{1}{k_B V T} \left\langle \sigma_V^2 \right\rangle. \tag{2}$$

The thermal expansion coefficient is proportional to the covariance of volume and enthalpy

$$\alpha = \frac{1}{k_B V T^2} \left\langle \sigma_{(V)(H)} \right\rangle. \tag{3}$$

(ii) Derivatives. The same quantities can be also obtained as the derivatives of the enthalpy and volume as follows [50, 51]

$$c_p = \frac{H(p, T+\epsilon) - H(p, T-\epsilon)}{2\epsilon}. \tag{4}$$

$$\beta = -\frac{1}{V(p,T)} \frac{V(p+\epsilon, T) - V(p-\epsilon, T)}{2\epsilon}. \tag{5}$$

$$\alpha = \frac{1}{V(p,T)} \frac{V(p, T+\epsilon) - V(p, T-\epsilon)}{2\epsilon}. \tag{6}$$

(iii) Density of states. Constant volume and pressure specific heat capacities (c_v and c_p respectively) are related to one another via:

$$c_p = c_v + \alpha^2 B V T \tag{7}$$

where α is the volumetric thermal expansion coefficient, V the volume, T the temperature and B the isothermal bulk modulus.

Considering a solid as an assembly of harmonic oscillators, the frequency distribution $S(\nu)$ is equivalent to a partition function. Then the constant volume heat capacity c_p can be calculated using Debyes relation

$$c_v = k_B \int_0^\infty \frac{\left(\frac{h\nu}{k_B T} \exp\left(\frac{h\nu}{k_B T}\right)\right)^2}{\left[\exp\left(\frac{h\nu}{k_B T}\right) - 1\right]^2} S(\nu) d\nu \tag{8}$$

with $\int S(\nu) d\nu = 3N$, where N is the number of atoms in the system.

The vibrational density of states (DoS) is obtained from the atomic velocity autocorrelations with quantum statistical corrections as shown above. The $S(\nu)$ is found as a sum of vibrational normal modes [41, 52]

$$S(\nu) = \frac{2}{k_B T} \sum_{j=1}^{N} m_j \left(\sum_{k=1}^{3} s_j^k(\nu) \right) \tag{9}$$

where the spectral density of atom j in the k-th coordinate and can be determined from the square of the Fourier transform of corresponding velocity $u_j^k(t)$

$$s_j^k(\nu) = \lim_{\tau \to \infty} \frac{1}{2\pi} \left| \int_{-\tau}^{\tau} u_j^k(t) \exp\left(-i 2\pi \nu t\right) dt \right|. \tag{10}$$

In the following three subsections we will discuss the application of these methods to the estimation of the bulk modulus, coefficient of thermal expansion, and heat capacity in the molecular dynamical simulations and comparison of the obtained values with the available experimental data.

4.5 Estimation of the bulk modulus

Another important parameter in eq. (7) is the bulk modulus B. The Bulk Modulus describes the elastic properties of a solid or fluid when it is under pressure on all surfaces. The applied pressure reduces the volume of a material, which returns to its original volume when the pressure is removed. In fact, the bulk modulus is a measure of the ability of a substance to withstand changes in volume when under compression on all sides. The bulk modulus is defined as

$$B = -\left(\frac{1}{V}\frac{dV}{dP}\right)^{-1}$$

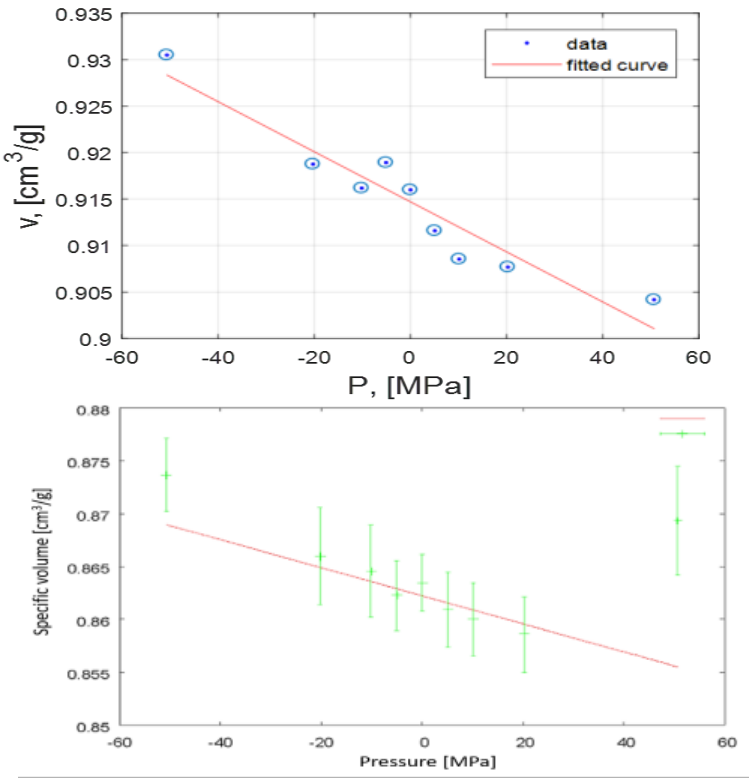

Figure 14: Specific volume as a function of applied pressure used for direct measurements of the bulk modulus for PC (top) and PEI (bottom).

Our earlier preliminary results of the estimations of the bulk modulus for small samples of amorphous PC and PEI cells were based on J-OCTA code and are shown in the Fig. 14. The estimated values of the bulk modulus after 400,000 steps at each pressure point are: (i) 4.17 GPa for PEI and (ii) 3.4 GPa for PC.

To improve these estimations we note that the recommended/verified by J-OCTA number of steps is 1,000,000 and the recommended

degree of polymerization for PEI is ≥ 12 and for PC ≥ 20. We note that the degrees of polymerization in our simulations are restricted by the constraints on the total number of atoms. Therefore, in our more accurate estimations reported below, we aimed to extend the integration time by an order of magnitude.

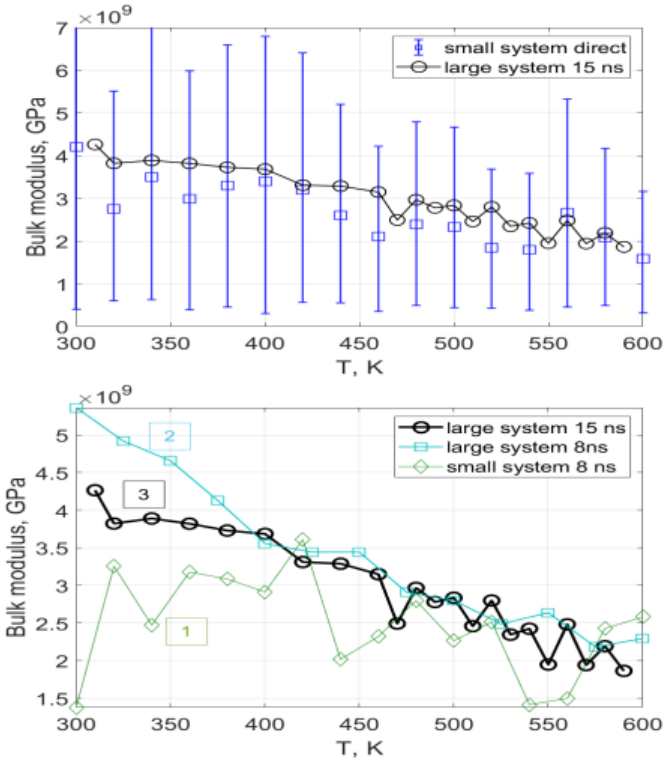

Figure 15: (top) Bulk modulus estimated as a function of temperature (blue open squares) using direct MD measurements for a small sample. Vertical bars indicate 95% of confidence bounds. B as a function of temperature (black open squares) estimated using fluctuations in GROMACS. (bottom) The results of the convergence analysis for the bulk modulus estimations: (1) small system after 8 ns integration time; (2) large system after 8 ns of integration; (3) large system after 15 ns of integration.

The results of GROMACS calculation of the bulk modulus of PEI/PC blend as a function of temperature are shown in Fig. 15 (top). To obtain these estimations we used 9 values of the pressure as shown in Fig. 14 for each temperature. The direct MD calculations of B were further compared with the MD predictions based on fluctuational formula (2). The results of the MD calculations of the bulk modulus are shown by the black open circles in the figure.

It can be seen from the figure that estimations based on fluctuations are in good agreement with direct measurements and apparently are

less dispersed. It is also worth mentioning that GROMACS calculations used to obtain the black line in the figure are much faster than direct measurements and provide simultaneous estimation of other thermodynamic variables of the system. For this reason in what follows, we will use mainly results of the GROMACS estimations.

4.5.1 Convergence

To use GROMACS estimations it is very important to analyze the convergence of the results both as a function of system size and time of integration. Although detailed analysis of this kind is very expensive, we have investigated two systems - small (5,166 atoms) and large (41,328 atoms) for different integration times ranging from 1 to 16 ns. Some results of such analysis are shown in Fig. 15 (bottom). As we have explained above the curve (3) in this figure is in good agreement with the results of direct measurements. It was obtained using fluctuations and 15 ns integration time in the large system. We therefore were using measurements with 15 ns integration time in the large system as a baseline for our estimations.

4.5.2 Comparison with the experiment

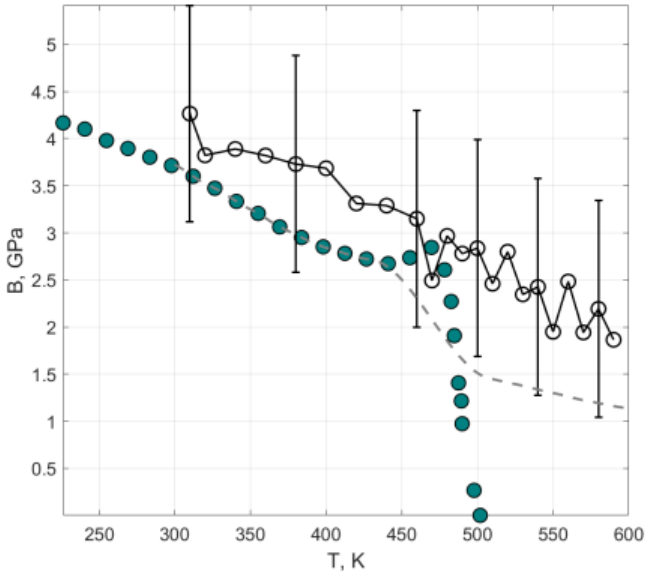

Figure 16: Bulk modulus obtained using MD simulations (maroon diamonds) as compared to the experimental data obtained for ULTEM 1000 [29] (teal circles). Vertical bars show error estimates. The dashed gray line indicate educated guess of expected behavior of experimental bulk modulus above glass transition temperature.

We now compare the results obtained for large system with experimental data. The MD simulations for large system after 15ns of integration for each temperature point shown in Fig. 16 by open black circles are the same as in the Fig. 15 (bottom). The experimental data are shown by the teal circles.

We note that Prospector website [29] provides only data for tensile modulus as a function of temperature. To estimate bulk modulus we use nominal value of the Poisson ratio ~ 0.36 and the following conversion

$$B = \frac{E}{3(1-2\nu)}.$$

We also note that the tensile modulus is available only in the glass state and drops to zero above the glass transition temperature. Therefore, the comparison is only available for $T < T_g$.

The results of comparison are shown in Fig. 16. The figure demonstrates a reasonable agreement with experimental data in the low temperature region. The expected behavior of the bulk modulus above the glass transition temperature is shown in the figure by dashed gray line. The educated guess is based on the data reported in [41, 53]. This behavior is expected due to the fact that Poisson ratio above glass transition temperature is quickly approaching 0.5 [53]. And its growth compensates the decay of modulus according to equation above. It is also well known that compressibility of liquids does not significantly deviate from compressibility in these polymersin glass state.

To conclude this section, we note that estimated values of the bulk modulus are in reasonable agreement with experimental data and the results of earlier MD simulations in similar materials [41]. We now proceed to the discussion of the MD results obtained for thermal expansion coefficient.

4.6 Estimation of the thermal expansion coefficient

For MD estimations of the thermal expansion coefficient we followed the same guiding lines discussed in the previous section. The results of the estimation of the thermal expansion coefficient using thermal fluctuations (2) are shown in Fig. 17 (top) in comparison with the results of estimation based on the derivative of specific volume (6). The comparison shows that the results based on the derivative approach those based on fluctuations for large sample after 15 ns of integration time.

We note that the temperature dependence of thermal expansion coefficient follows the expected trend. The values of the α_P are in agreement with earlier MD estimations in similar materials [41]. Estimated value of α_P at room temperature is approximately 2.5 - 3 times larger than reported values for linear thermal expansion coefficient of ULTEM 9085. It is in a good agreement with expected factor of 3.

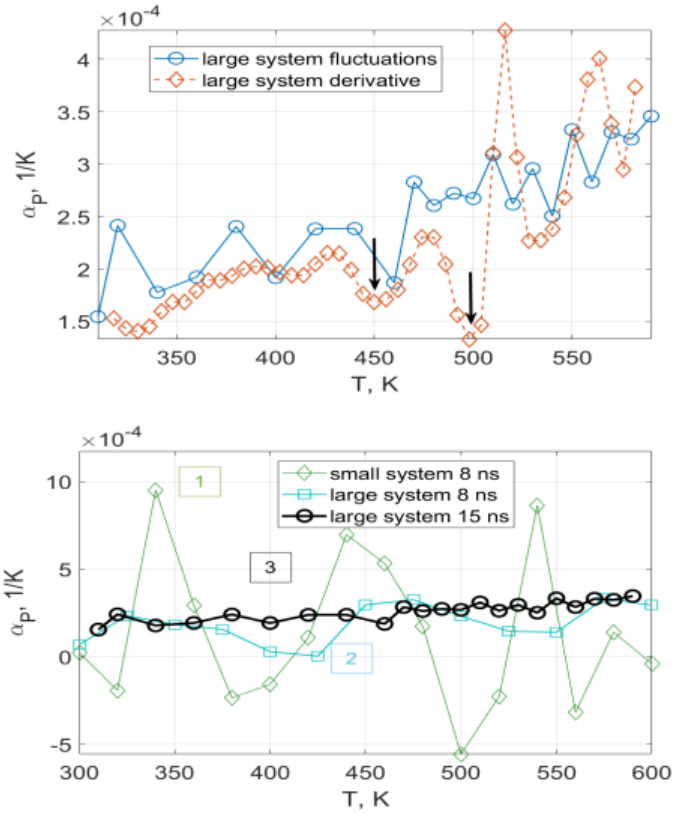

Figure 17: (top) Thermal expansion coefficient estimated as a function of temperature using derivative of specific volume (brown open diamonds) in a large system while heating it up, see Fig. 31. α_P as a function of temperature (blue open circles) estimated using fluctuations in this system. (bottom) The results of the convergence analysis for the estimations of thermal expansion coefficient from the fluctuations: (1) small system after 8 ns of integration time; (2) large system after 8 ns of integration; (3) large system after 15 ns of integration. Black arrows show the location of the changes in the changes in α_p response to the temperature increase that are related to the initiation of the glass transition.

We note, in addition, that the results obtained using direct measurements for the thermal expansion coefficient allows one to estimate T_g. In particular, the features indicated by the arrows in the Fig. 17 (top) can be interpreted as the initiation of the changes in the system response to the temperature increase. These features correspond to the glass transition temperature estimation of T_g value somewhere between 470 and 510 K.

Further evidence of the phase transition may be obtained from the MD analysis of the specific heat capacity and its comparison with ex-

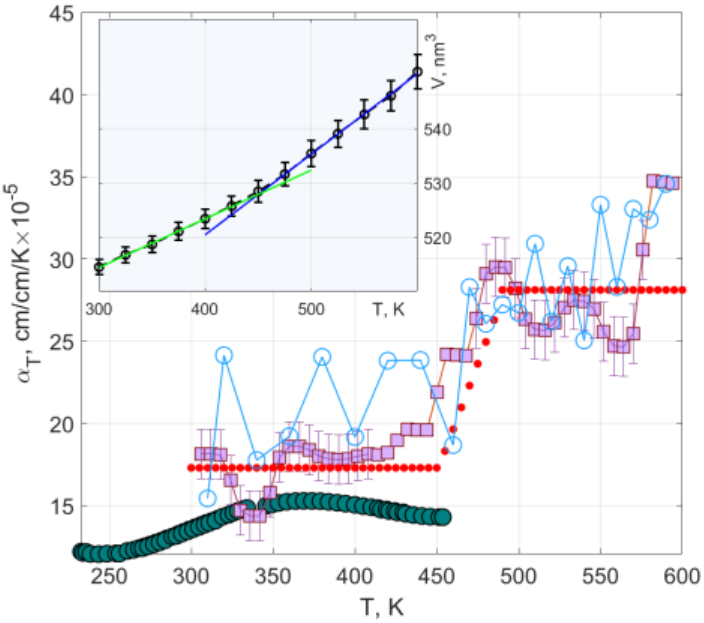

Figure 18: Thermal expansion coefficient estimated as a function of temperature using derivative of specific volume (maroon shaded squares) in a large system during quenching, see Fig. 31. Red dotted horizontal lines correspond to the estimations based on the linear fit of the volume variation as a function of temperature shown in the inset. Blue open circles show α_T found using fluctuations (the same as in Fig 17 top). Experimental data (teal shaded circles) obtained for ULTEM 1000 [29]. Piece-wise linear approximation to the linear fit is shown by red dots.

perimental results as discussed below.

4.6.1 Convergence

The convergence of the estimations based on fluctuations is shown in the Fig. 17 (bottom). The convergence results follow the same trend as the results obtained in the analysis of the bulk modulus. The comparison between the two estimations (for the bulk modulus and the coefficient of thermal expansion) confirm our earlier conclusion that measurements based on 15 ns integration time in the large system can serve as a base estimation of thermodynamic and mechanical properties in our system.

4.6.2 Comparison with the experiment

Experimental data for the coefficient of linear thermal expansion are available on the Prospector website [53]. To compare these data with

the results of simulations we notice that the volumetric thermal expansion coefficient estimated in the MD is three times the linear coefficient.

The comparison of the MD predictions with the corrected experimental data is shown in Fig. 18. The experimental data are only available for the temperature below glass transition temperature. In this region the MD predictions demonstrate good agreement with experimental data. A slight shift of the predicted data towards higher values is expected in PEI/PC blends as compared to pure polyetherimide since polycarbonate α_P as compared to PEI.

Another very important feature of the α_P can be observed in the figure. The inset of the figure shows abrupt change in the slope of the volume as a function of temperature at the glass transition. Below and above glass transition temperature the slope remains nearly constant. This is the well-known feature of polymer melts [41] that corresponds to the jump in coefficient of thermal expansion at T_g.

We note, however, that measurements of the jump during different stages of the thermal cycling (see Fig. 31) do not allow to determine uniquely the location of the jump and the jump value. The value of the T_g estimated in these measurements ranges between 450 and 500 K and the value of the jump ranges from 5 to 10 $cm/cm/K \times 10^{-3}$.

The constant slopes in the inset correspond to the horizontal red dotted lines in the figure. The jump at T_g is clearly seen. This jump is the only jump corresponding to the glass transition clearly resolved in molecular dynamics simulations. In particular, it underlies in accordance with eq. (7) the weak jump observed in specific heat capacity at constant pressure as will be explained in details the next section.

4.7 Estimation of the density of states

Estimations of the density of states for the OPLS-AA force field with quantum corrections are shown in comparison with experimental Absorption spectra in Fig. 19 (left). The results presented in the Fig. 19 were obtained using LAMMPS. The density of states were estimated by computing the mass weighted velocity autocorrelation functions for each atom type.

The comparison of the IR absorption spectra obtained in MD simulations with experimental data is shown in Fig. 19 (bottom). These spectra were obtained by calculating the autocorrelation function of the total dipole moment. The calculated spectra are in reasonable agreement with experimental data. In particular, one can see that the accuracy of the MD predictions based on the OPLS-AA force field (see Fig. 10 top line) has been improved by introducing quantum corrections to this force.

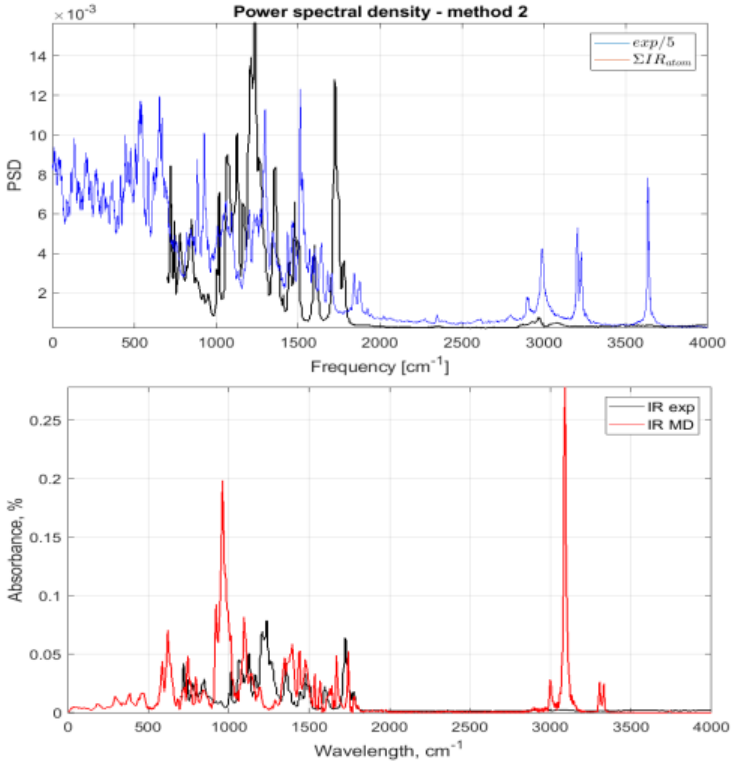

Figure 19: (left) Vibrational spectra (blue line) calculated as a mass-weighted sum of the velocity auto-correlation functions for all atom types in amorphous sample of PEI/PC blend; (bottom) Infrared spectra (red line)of the same sample calculated using auto-correlation function of the total dipole momentum. Black line in both figures correspond to the experimental IR spectra of ULTEM 9085 provided by MSFC.

4.8 Specific heat capacity - estimations

To calculate specific heat at constant volume and pressure we apply three methods discussed in Sec. 4.4.

Calculations of the specific heat of amorphous polymer sample based on fluctuations and derivatives of the total enthalpy were obtained by heating or cooling the system using GROMACS simulations in NPT ensemble.

Following our pattern of analysis, we first compare the results of MD estimations of c_p based on the analysis of fluctuations (1) with the estimations based on the derivative of the Enthalpy (4) shown in Fig. 20 (top).

4.8.1 Convergence

The results of the convergence analysis are shown in Fig. 20 (bottom). We note that despite 15 ns integration time the values of c_p obtained

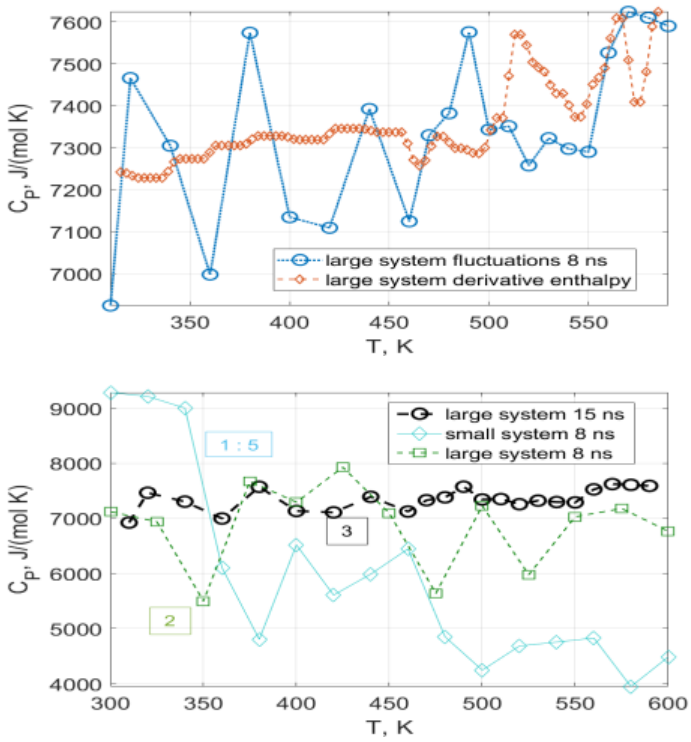

Figure 20: (left) c_p estimated as a function of temperature (blue open circles) using fluctuation analysis in the large sample after 8 ns integration time at each temperature. c_p as a function of temperature (brown open diamonds) estimated using derivative of the enthalpy. (bottom) The results of the convergence analysis of the estimations of c_p based on fluctuations: (1) small system after 8 ns integration time; (2) large system after 8 ns of integration; (3) large system after 15 ns of integration.

from fluctuations do not converge below glass transition temperature. We believe that this is due to the exponentially slow relaxation time in the system below T_g. As the result the pressure fluctuations that enter the enthalpy remain very large.

We note that the values of c_p obtained for the small sample differ by the factor of 5 from the values obtained for the large sample. In addition, the slope of the c_p curve obtained for the small sample is negative in contradiction to the experimental data and theoretical expectations. These issues highlight the difficulties related to the MD measurements of specific heat and set c_p estimations apart from estimations of other thermodynamic parameters.

4.8.2 Comparison with the experiment

The difficulties related to the MD estimations of the specific heat capacity are further highlighted by comparison the values of c_p predicted by MD with the experimental data shown in Fig. 21. First, we notice that the fluctuation based values of c_p have to be reduced by approximately 50% ($\sim$ 3000 J/mol/K) to be comparable with experimental data. Secondly, we notice that initiation of the glass transition indicated by the arrow in the figure is shifted to the higher temperatures by $\sim$ 50 K. Note, that similar shift was observed in the earlier MD simulations of similar polymer systems [41].

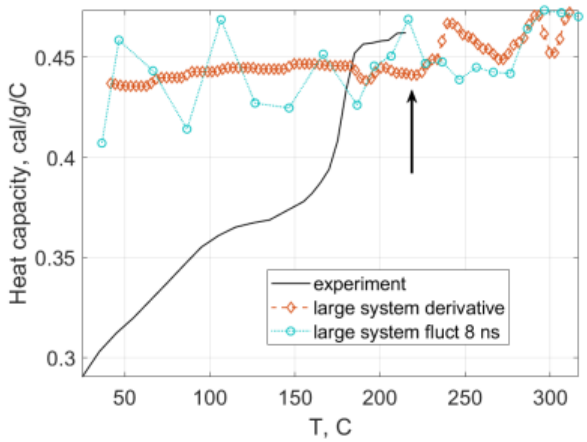

Figure 21: Comparison of the fluctuation and derivative based predictions for the values of c_p (open symbols the same as in Fig. 20 (top)) with experimentally measured quantities (black solid line provided by MSFC). The black arrow indicates the initiation of the glass transition.

The discrepancy between experimental data and the values of c_p estimated using fluctuations and derivative of the enthalpy can be attributed e.g. to the luck of quantum corrections that are usually considered in estimations of c_v values [41, 52].

We included the quantum corrections using equation (7), where c_v was calculated following eqs. (8)-(10). The calculations of the density if states were performed in GROMACS using subroutine "gmx dos". The values of the thermal expansion coefficient α_T in the eq. (7) are the results of the piece-wise linear approximation shown by red dots in Fig. 18 discussed in Sec. 4.6. The values of the bulk modulus in the eq. (7) are those shown in the Fig. 16 by open circles.

The results of the corresponding calculations are shown in Fig. 22. Note that the values and the slope of the c_v (open blue circles) and c_p (asterisk) curves were indeed corrected using this theory. The shift in the onset of the glass transition is also corrected by including piece-wise linear approximation for the thermal expansion coefficient.

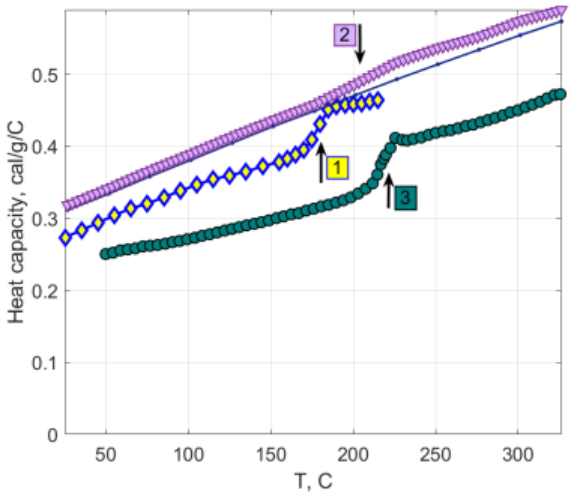

Figure 22: The results of the c_v (solid dotted line) and c_p (maroon triangles) MD calculations based on the estimation of the density of states including quantum corrections as compared to the experimentally measured quantities provided by MSFC for ULTEM 9085 (yellow shaded diamonds) and by Prospector website for ULTEM 1000 [29] (teal shaded circles). Black arrows show the initiation of the glass transition in the experiment and MD estimations of the heat capacity.

To conclude this section we note that the obtained results despite some remaining discrepancies provide reliable validation of the atomistic approach chosen in this research for analysis of the welding dynamics at polymer-polymer interface. In the remaining sections of this report, we will discuss the results of the analysis of the shear viscosity in large samples with flat polymer-polymer interface.

5 Polymer-polymer interface - large sample

To build polymer-polymer interface we prepared two polymer cells. The polymer chains were placed at random into the cell with z-size ≈ 70 Å (nearly equal to the length of the polyetherimide chain) and the size of the (x, y) cross-section $\approx 60 \times 60$ Å corresponding to the sample density $\approx 1 g/cm^3$.

The surface of each sample was prepared by moving polymer chains inside each cell at a given interface and using non-periodic boundary conditions in Z-direction and a LJ-wall to keep the polymer chains away from the interface during the preparation. The parameters of the LJ-wall at the interface were: (i) cut-off ~10 Å; (ii) sigma ~5 Å; (iii) epsilon ~10 kJ/mol; and (iv) density ~20 g/cm^3.

Both cells were relaxed using the procedure developed by the J-OCTA($T_0 = 600$ K and $P_0 = 1$ atm)

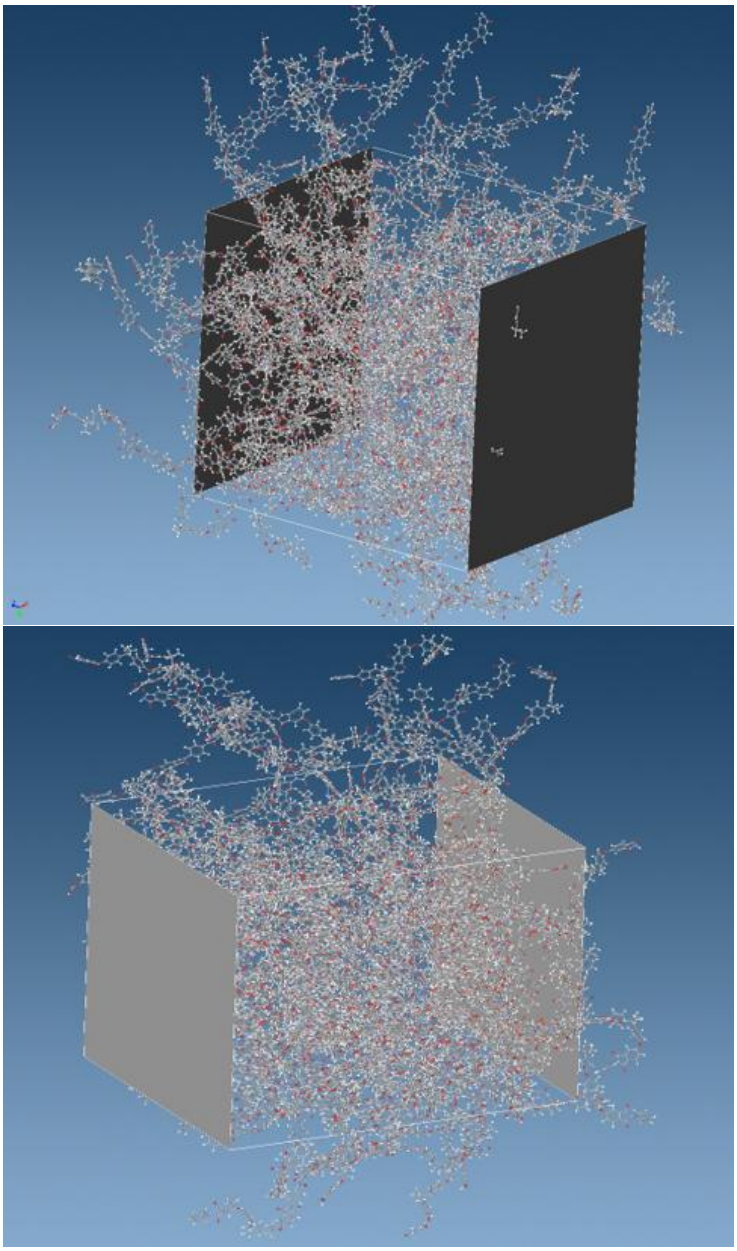

Figure 23: Fully atomistic amorphous cells of PEI/PC polymers blends. Each polymer had 5 repeating monomer units. PEI unit has 70 atoms PC unit has 35 atoms. Each cell contains 48 PEI and 24 PC polymers. (top) Cell with flat interface on the right (bottom) cell with flat interface on the left.

nve_equil_in.in We use NVE equilibration at a given temperature, e.g. T_0;

compress.in The equilibration is followed by compression in the NPT Andersen-Nose-Hoover thermostat at T_0 and $P = 100$ MPa;

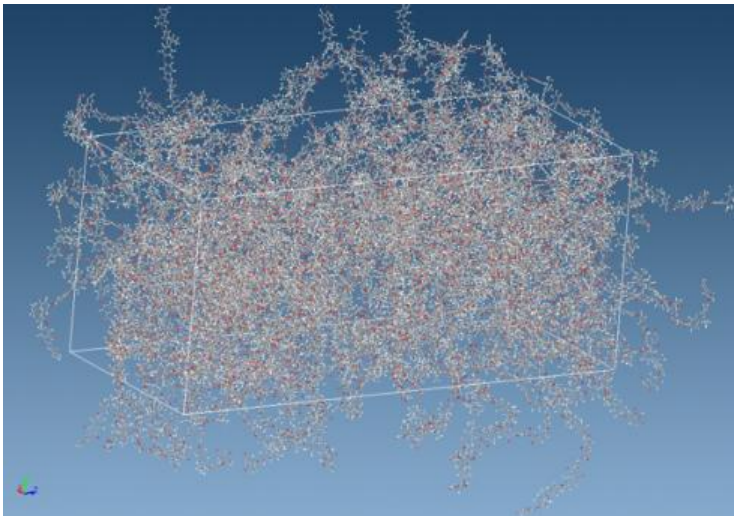

Figure 24: Two fully atomistic amorphous cells of PEI/PC polymers blends combined in one chemical sample with atomistically flat polymer-polymer interface.

nve_equil_after_compress_in.in The compression is followed by equilibration in the NVE equilibration at T_0;

equil_in.in

nvt_equil_in.in The equilibration is followed by relaxation in the NPT Andersen-Nose-Hoover thermostat at T_0 and P_0;

nvt_eliminate_trans_in.in Finally, the translational component of the velocity is eliminated in the NVT Nose-Hoover thermostat at T_0 and zero pressure.

Each step is computed during 50,000 steps with time step of 1 fs in LAMMPS.

The initial amorphous cells are shown in the figure 23. The resulting amorphous cell is shown in the figure 24. The calculations were performed following general scheme sketched in the Fig. 25. The sample with planar interface was allowed to equilibrate in the NPT ensemble that keeps pressure, temperature, and the total number of particles fixed similar to the actual experimental conditions [2]. This process is shown by the green "Healing" arrow in the figure.

At some fixed time instances the sample was quenched to the room temperature as shown in the figure by the blue vertical lines. The quenching was also accomplished using NPT ensemble. The quenched samples were used for measurements of the shear viscosity.

[2] Note that the temperature can be considered nearly fixed during 300 ns used in MD simulations.

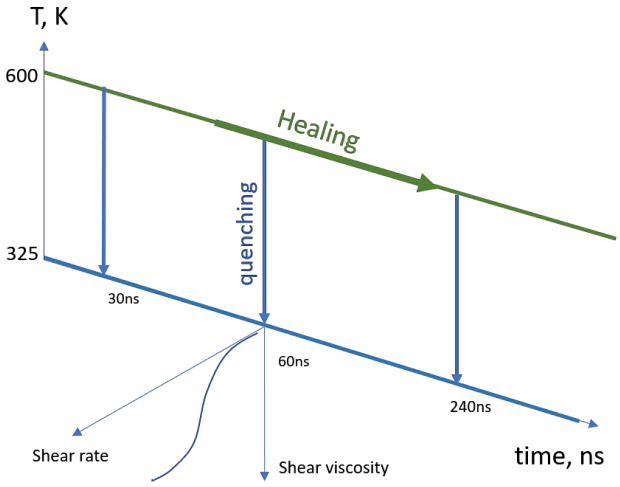

Figure 25: Sketch of the calculation scheme. Green arrow shows healing at constant temperature (600 K) and pressure (1 atm) during 300 ns. The quenching of the sample at some fixed time instances is shown by blue vertical arrows. The measurements of the shear viscosity of quenched samples is illustrated by additional pair of axis in the end of the quenching process.

5.1 Interface welding

The process of the inter-diffusion of the polymer chains at the interface is illustrated in Fig. 26 and 27. Initially both sides (gray and cyan in the figure) have atomistically flat interfaces. As time proceeds the polymer chains on both sides diffuse across the interface in a warm like manner. The simplest form of this process is described by the reputation theory [54]. However, this theory does not account for the charge and rigidity of the polymer chains.

So far the polymer-polymer interface were analyzed using coarse-grained molecular dynamics [18, 20, 21, 55, 56]. Although rigidity of the polymer chains can be added to the coarse-grained model [56] the electrostatic effects [57] are not included, and the overall limited accuracy of the coarse-grained models does not allow for direct comparison with the experiment.

The focus of the present research is the direct comparison of the model predictions with experiment. At present, the only known approach to direct comparison of the results of MD simulations with experiment is to use fully atomistic model of the polymer melts [41, 51].

Accordingly, in this research we adopted an approach based on the development of a fully atomistic model of the polymer-polymer interface. The model used in the research is the result of extensive numerical experimentation that was aimed to resolve trade-offs in the parameter space of the problem: (i) length of the polymer chains (degree of

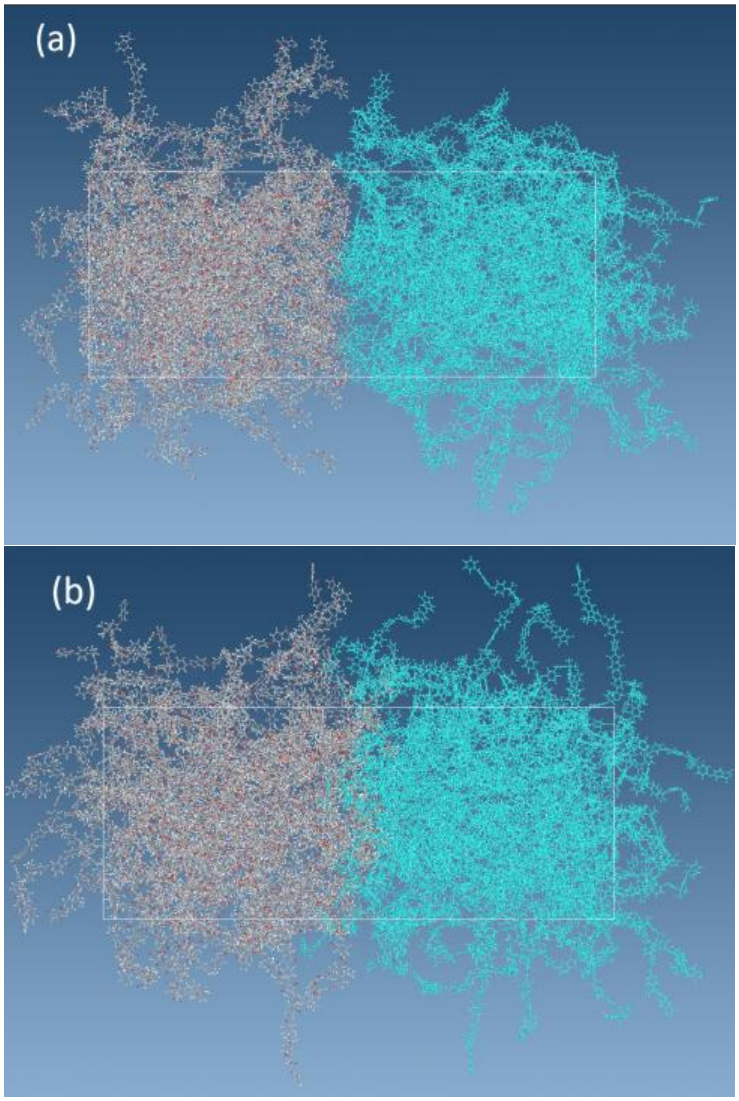

Figure 26: Visualization of the chain topology at the interface during the healing process. (top) Initial state with atomistically flat interface. (bottom) Mutual penetration of the chains after welding during 60 ns.

polymerization); (ii) length of the simulation box; (iii) total number of atoms; (iv) computer wall time per 1 ns of simulations.

The last parameter is at present the major limiting factor of the MD based approach. It limits the total number of atoms that can be used in the model. An extensive experimentation has shown that at present the total number of atoms that can be modeled is $\leq$ 45,000. The corresponding integration time is around 25 - 35 ns per day if accurate electrostatic calculations are used. As a result the length of the polymer chain (that should be $\lesssim$ side of the box) was limited to 5 repeating units of the polyetherimide. And the corresponding length of the box in

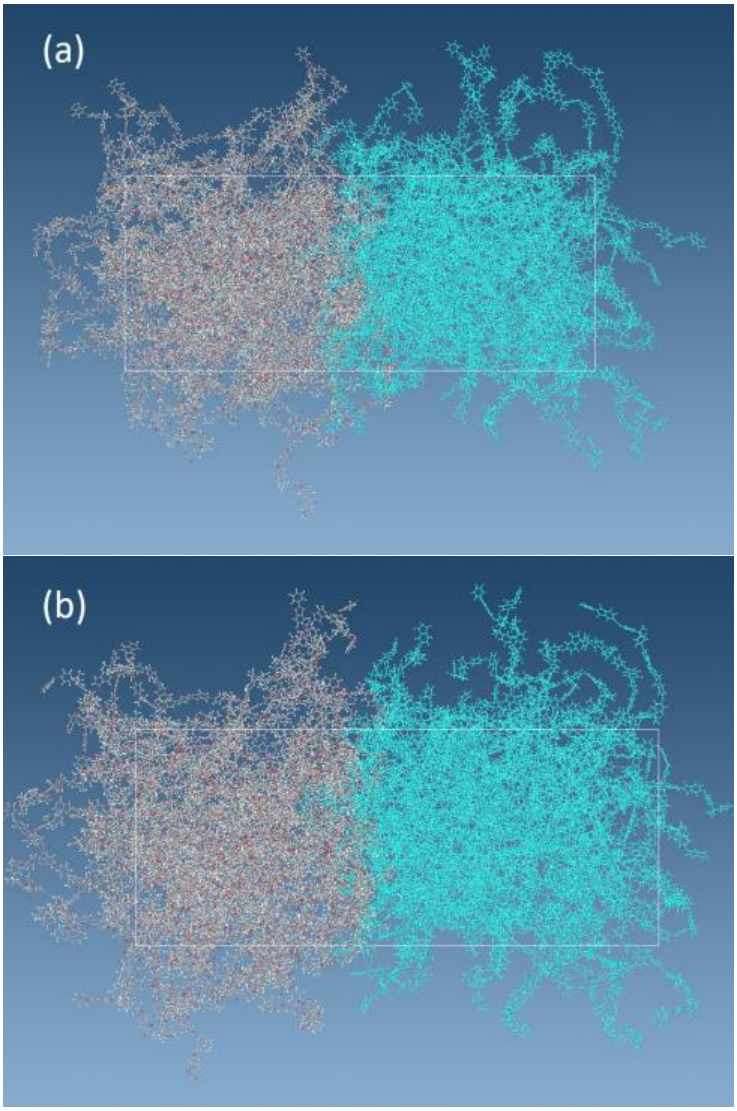

Figure 27: Visualization of the chain topology at the interface during the healing process. Mutual penetration of the chains after welding during: (top) 120 ns; and (bottom) 240 ns.

the direction normal to the interface was around 74 Å. The side length of the interface plane was around 60 Å.

The total diffusion time was limited by approximately 300 ns. After that time the effect of the periodic boundary conditions (i.e. effect of the boundaries on the dynamics at the interface) becomes important.

5.2 Expected behavior

The conventional point of view [58–60] on welding at the interface is presented in Fig. 28. As two polymer samples are allowed to equili-

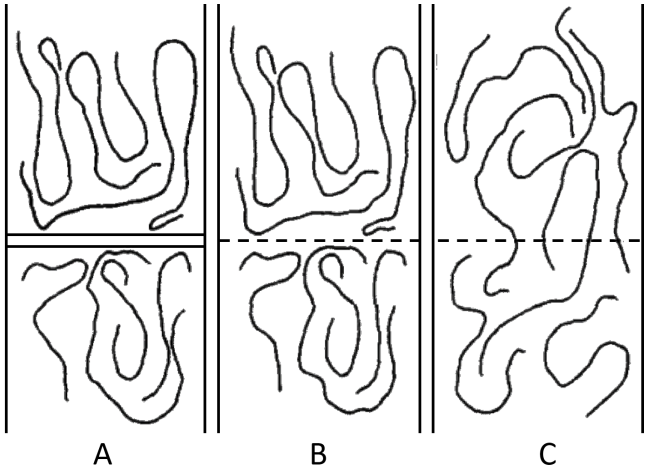

Figure 28: Conventional point of view of chains diffusion at the interface.

brate at the polymer-polymer interface at 600 K, the first observed phenomenon is "wetting" when two surfaces quickly come close to each other. In the Fig. 28 the initial gap is shown in the panel A.

The wetting process is governed by the electrostatic and van der Waals forces. The closer the surfaces are to each other, the larger is the energy of interaction and the smaller is the total nonbonding energy. The process of decreasing the nonbonding energy continues as reptation of the polymer chains at the interface progresses. We therefore expect to see a continuous decrease of the total non-bonding energy of the sample as a function of welding time. The rate of relaxation of non-bonding energy is expected to decrease with time.

This effect can be clearly seen in a small sample in which the surface contribution to the non-bonding energy is relatively large.

According to Eyring theory of surface viscosity μ its value is significantly different from the bulk value [61, 62]. For the flow of a surface molecule to occur, this molecule must acquire the energy of activation necessary to pass over the potential barrier which separates it from the neighboring equilibrium position [61, 62]

$$\sinh\left[\frac{\mu^s\left(dv_y/dx\right)A_m}{2k_BT}\right]=\left[\frac{\left(dv_y/dx\right)h}{2k_BT}\right]\exp\left(\frac{\Delta G}{k_BT}\right)$$

where v_y is the velocity of the molecule in direction parallel to the surface, A_m is the molecular area, k_B is Boltzmanns constant, R is gas constant, $\hbar$ Plancks constant, T is temperature and $\triangle G$ is the free energy of activation.

In Eyring's theory, the flow of a monolayer remains Newtonian as long as the following inequality is satisfied. This expectation is also

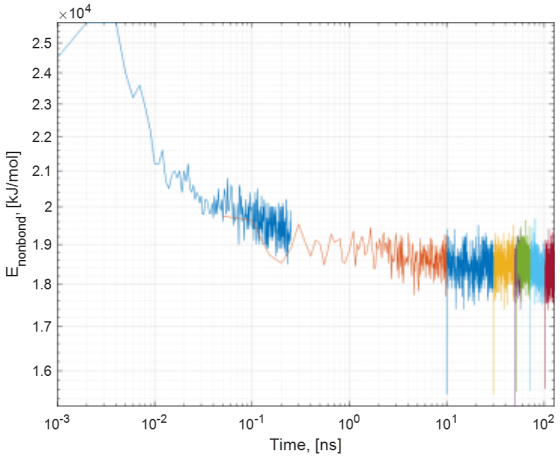

Figure 29: Relaxation of non-bonding energy as a function of time in a small sample.

intuitively clear on the ground that shear viscosity of impaired sample must approach bulk value after sufficiently large welding time.

$$\left[\frac{\mu^s\left(dv_y/dx\right)A_m}{2kT}\right] \ll 1 \qquad \text{and} \qquad \mu^s = \frac{h}{A_m}\exp\left(\frac{\Delta G}{kT}\right).$$

According to this view, the initial structure of the polymer-polymer interface with nearly atomistically flat surfaces corresponds to $\triangle G \sim 0$ and a very small surface viscosity resulting in slippery conditions at the surface. The small surface viscosity should also be reflected in the reduced total viscosity measured by e.g. non-equilibrium molecular dynamics with shear deformation applied in the plane parallel to the interface.

We therefore expect that the total viscosity will increase with increasing diffusion time.

5.3 Quenching large system

To estimate the change of the total shear viscosity as a function of time, we quench the large model at two different time instances 60 ns and 240 ns of welding.

The results of quenching are shown in Fig. 30. It is performed in 12 steps of 25K each using NPT ensemble at pressure 1 atm. Only 11 steps are shown in the figure because shear viscosity was measured at the temperature of 325K. The resulting samples at different temperatures were used to estimate thermodynamic properties of the PEI/ PC blend, see Sec. 4.

The overall thermal history of the large PEI/PC sample is shown in Fig. 31. The initial welding of the sample at $T = 600$K during 240 ns is

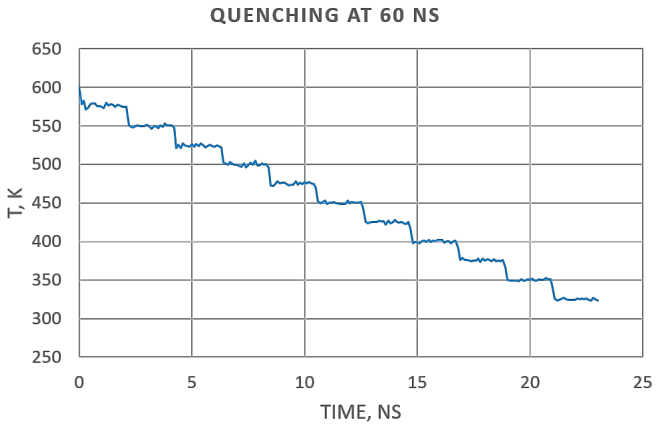

Figure 30: Quenching large system after 60 ns of healing.

followed by fast quenching to 300K in 23 ns similar to the quenching shown in Fig. 30. Quenching is followed by slow heating in 21 steps with time step varying between 10 and 25 ns. Finally, the system was slowly cooled in 24 steps with time step varying between 12 and 25 ns. The system was above glass transition temperature for approximately 590

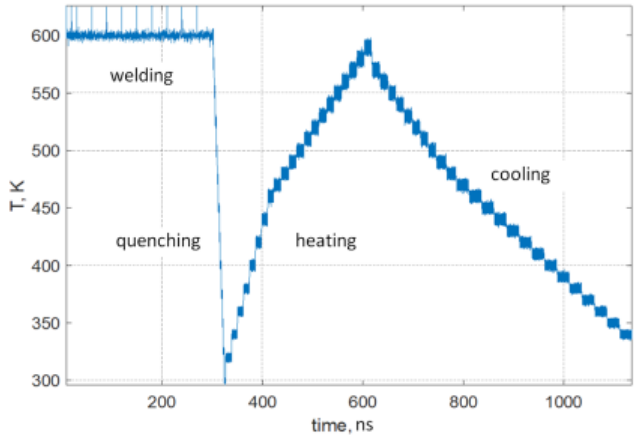

Figure 31: Temperature profile of the large sample. Left to right: (i) welding at constant temperature; (ii) fast quenching; (iii) ”slow” heating; and (iv) ”show” cooling of the sample.

Below we describe the results of the measurement of the shear viscosity. These are central results of the project.

5.4 Elongation analysis using Molecular Dynamics

J-OCTA allows one to use the molecular dynamics engine to evaluate mechanical properties (uniaxial elongation). The actual calculation

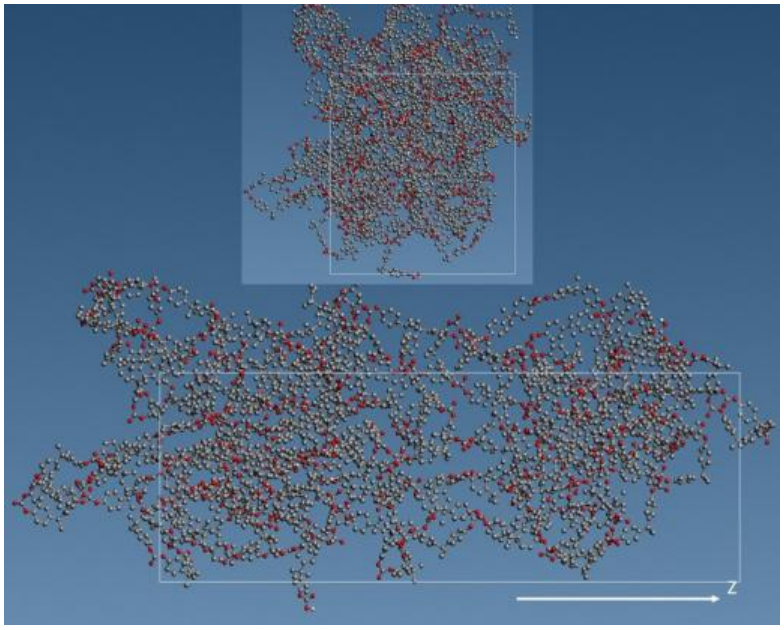

Figure 32: Molecular dynamics simulations of elongation in polycarbonate. The snapshots of the initial cubic sample (at the top - not in scale) and the fully elongated sample (bottom).

procedure involves applying a deformation (simple elongation) at constant rate in the Z-axis direction with respect to a system created previously. A stress-strain diagram is displayed when the calculations are complete. The Young's modulus, yield stress, and post-yield behavior can be evaluated from this diagram.

The pressure tensor [3] is calculated as [50, 64, 65]

$$\sigma_{ij} = \frac{1}{3V}\left\langle \sum_{k\in V} m^{(k)}\left(u_i^{(k)} - \bar{u}_i\right)\left(u_j^{(k)} - \bar{u}_j\right) + \frac{1}{2}\sum_{l\in V}\left(x_i^{(l)} - x_i^{(k)}\right) f_j^{(kl)} \right\rangle \qquad (11)$$

here

- k and l are atoms in the domain
- V is the volume of the domain
- $m^{(k)}$ is the mass of atom k
- $u_i^{(k)}$ is the i-th component of the velocity of atom k
- $\bar{u}_j$ is the j-th component of the average velocity of atoms in the volume
- $x_i^{(k)}$ is the i-th component of the position of atom k
- $f_i^{(kl)}$ is the i-th component of the force applied on atom k by atom l

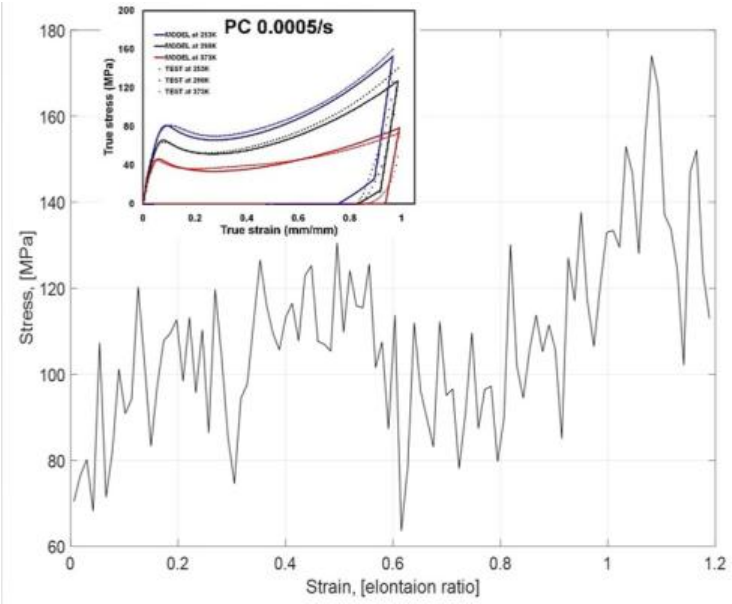

Figure 33: Molecular dynamics simulations of elongation in polycarbonate. The strain stress curve obtained from MD simulations (jiggling line) as compared to the experimental strain stress curves shown in the inset.

5.4.1 Elongation of the bulk amorphous PC sample.

We consider first the results of the calculation of the strain stress curve in the bulk sample of polycarbonate. The sample contained 4 chains of polycarbonate. Each chain contains 950 atoms. Simple elongation is applied in z-direction with constant rate. The results of the simulations obtained for room temperature with elongation rate 5000 cm/sec are shown in Fig. 32 and Fig. 32.

It can be seen from the figures that there is a semi-quantitative agreement between the predictions obtained using MD calculations and the experimental results. In particular, the overall shape and approximate values of the strain and stress obtained in MD simulations are in agreement with the experiment. However, it can also be noticed that there some discrepancies in the location of the peak and its value.

We also note large fluctuations of the stress in the Fig. 32. The fluctuations can be reduced by increasing the size of the sample as will be shown below. There are several other factors that affect the outcome of simulations of the strain-stress curves. Among these factors are the time step of simulations, the elongation rate, and the assumption regarding the value of the Poisson's ratio ν. In particular, for the elongation in z direction J-OCTA offers to choose between $\nu = 0$ and $\nu \neq 0$. In the for-

[3]Recall that stress tensor σ_{ij} is defined [63] as $\sigma_{ij} = \left(\partial F/\partial \varepsilon_{ij}\right)_T$, where ε_{ij} is the strain tensor $\varepsilon_{ij} = 1/2(\partial u_i/\partial x_k + \partial u_k/\partial x_i)$ and $u_i = x_i' - x_i$ is the displacement vector.

mer case σ_{zz} is given directly by eq. (11) and the size of the simulation cell in x and y directions is assumed to be unchanged, while in the latter case the stress in z direction is calculated as $\sigma_{zz} - \frac{1}{2}(\sigma_{xx} + \sigma_{yy})$ and the change of the cell size in x and y directions is scaled as $(1 - \nu \cdot \varepsilon_{zz})$.

Here our main concern was to investigate generic capabilities of the MD for analysis of mechanical and spectral properties of PEI/PC melts during welding process at the interface. We therefore briefly consider only effect of some of the factors mentioned above, while detailed validation procedure will be described elsewhere.

5.4.2 Elongation of the large sample with plane interface.

Note, that the molecular dynamic simulations of a small sample can not accurately quantify the strain stress relation of the blends with planar interface. We, therefore, increased the size of the sample and changed the integration time step and elongation rate to enable comparison with the experiment.

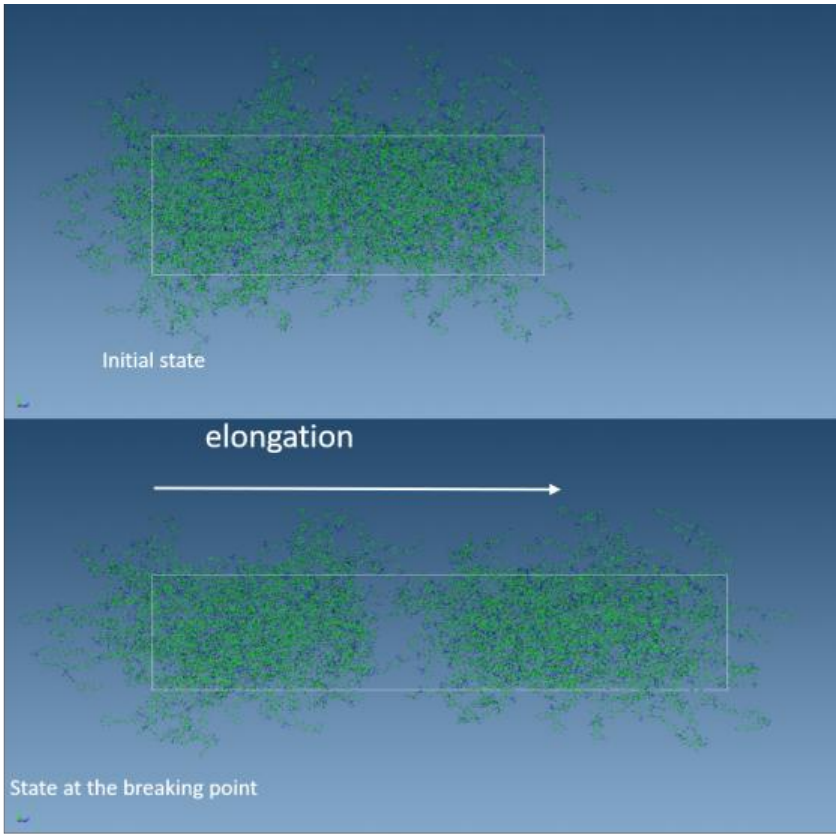

Figure 34: Results of elongation simulations obtained after 240 ns of welding in the large sample. The sample has a single interface between two PEI/PC blends in XY-plane. The top panel shows initial state and bottom panel shows final state of the sample.

First, we perform measurements of the elongation by resolving the breaking-up dynamics as shown in Fig. 34. The results of preliminary analysis are shown in Fig. 35 for three different welding times in comparison with the experimental curve. The simulations were done using J-OCTA VSOP solver [31] with elongation rate 50 m/s and time step $dt = 0.5$ fs.

The following features can be seen from the figure. There is a weak increase of the Young's modulus and the Yield strength as a function of the welding time. Although this result is consistent with the expectations based on discussion in Sec. the observed difference between different curves is very small. In addition, the MD curves deviate from the experimental data, the calculations were performed under assumption that the Poisson's ratio $\nu = 0.36$, which is not inaccurate as the sample begin to break up [66].

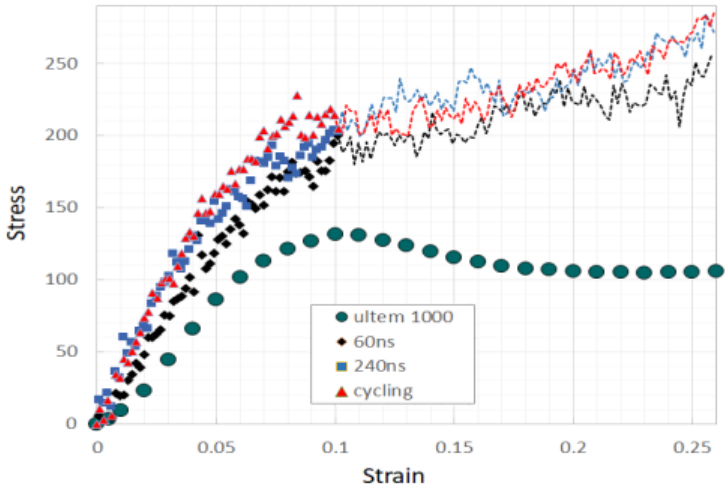

Figure 35: MD simulations of the strain-stress curves at 300 K (elongation rate 50 m/s, time step 0.5 fs) as a function of welding time: (i) 60 ns (diamonds); (ii) 240 ns squares; and (iii) after additional welding during temperature cycling (1200 ns). The curves are shown by dashed lines for large strains where assumption of constant Poisson ratio is not valid. The experimental data obtained by ULTEM 1000 [29] are shown by teal shaded circles.

Some of these issues are addressed below. As the second step of our analysis we verify the dependence of the MD results on the elongation rate. The comparison of the strain-stress curves obtained for three different elongation rates ranging from 50 m/s to 1 m/s are shown in Fig. 36. It can be seen from the figure that the stress-strain curve obtained in MD simulations gradually approach the experimental data as the elongation rate is reduced. Note, however, that the experimental elongation rate is approximately 4 orders of magnitude smaller than the smallest rate used in simulations, see the inset of the Fig. 33.

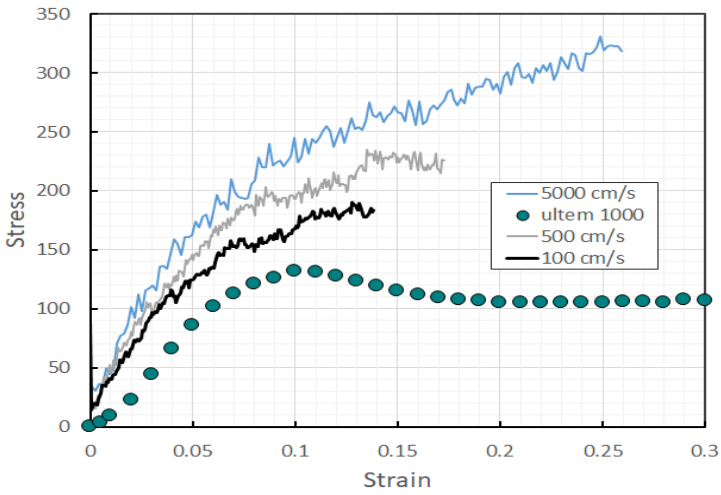

Figure 36: MD simulations of the strain-stress curves as a function of welding time: (i) 60 ns (diamonds); (ii) 240 ns squares; and (iii) after additional welding during temperature cycling (1200 ns). The experimental data obtained by ULTEM 1000 [29] are shown by teal shaded circles.

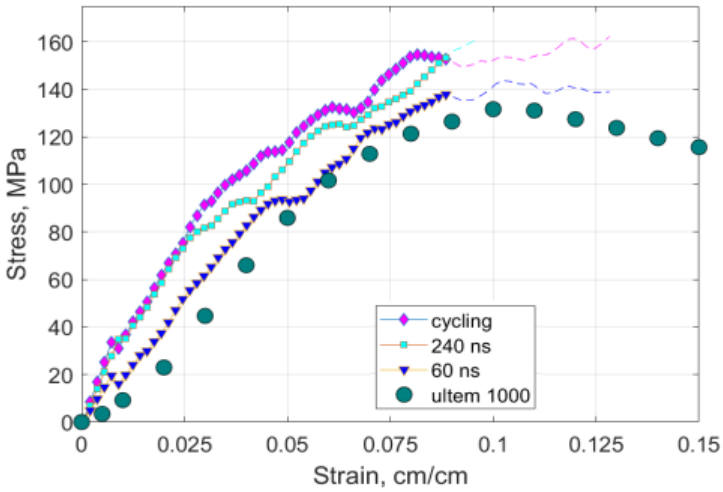

Figure 37: MD simulations of the strain-stress curves at 350 K (elongation rate 1 m/s, time step 0.25 fs) as a function of welding time: (i) 60 ns (diamonds); (ii) 240 ns squares; and (iii) after additional welding during temperature cycling (1200 ns). The curves are shown by dashed lines for large strains where assumption of constant Poisson ratio is not valid. The experimental data obtained by ULTEM 1000 [29] are shown by teal shaded circles.

Finally, we repeat the simulations shown in the Fig. 35 using slightly higher temperature (350 K) and substantially reduced elongation rate (1 m/s). We note that the results obtained in MD simulations with reduced elongation rate and increased temperature demonstrate better agreement with experiment. But the main tendency of the dependence of the MD strain - stress curves on the welding time is the same as in the Fig. 35: both the Young's modulus and the Yield strength increase as the welding time is increased.

The obtained value of the Young's modulus

$$E \sim 2\ GPa$$

is slightly smaller than the value 2 - 2.5 GPa estimated based using functional and some open data [67]. We note, however, that obtained value of the Young's modulus is in goof agreement with the data reported for ULTEM 1000 [29] shown in the figure by open brown circles.

It can be seen in the figure that the sample breaks up at the location of the interface indicating that the interface remains the weakest point of the whole structure.

6 Estimating shear viscosity as a function of time

6.1 Expected behavior

The expected response of the polymer melts can be described as follows (see e.g. Flow Properties of Polymers): "The shear thinning of polymer melts and solutions is caused by disentanglement of polymer chains during flow. Polymers with a sufficiently high molecular weight are always entangled and randomly oriented when at rest. When sheared, however, they begin to disentangle and to allign which causes the viscosity to drop.

The degree of disentanglement will depend on the shear rate. At sufficiently high shear rates the polymers will be completely disentangled and fully alligned. In this regime, the viscosity of the polymer melt or solution will be independent of the shear rate, i.e. the polymer will behave like a Newtonian liquid again. The same is true for very low shear rates; the polymer chains move so slowly that entanglement does not impede the shear flow. The viscosity at infinite slow shear is called zero shear rate viscosity (η_0). The typical behavior is ilustrated in the figure below that shows the dependence of the apparent viscosity, η, of a polymeric melt on shear rate."

Continuing the quotation above we find that "The behavior of fluids in the shear-thinning regime can be described with the power-law equation of Oswald and de Waele:

$$\tau = K(\gamma)\dot{\gamma}^n$$

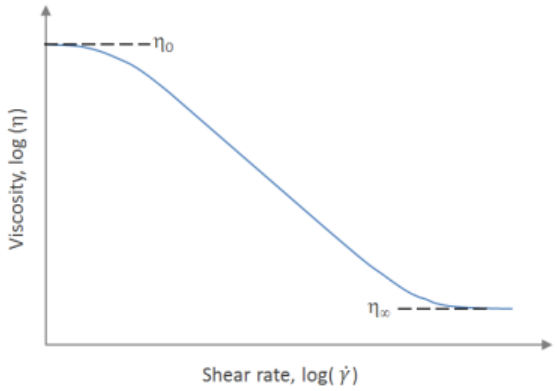

Figure 38: Expected shear-thinning of polymer melts, reprinted from [68].

This equation may be written in logarithmic form,

$$\log(\tau) = \log(K(\gamma)) + n\log(\dot{\gamma})$$

This means, a log-log plot of shear stress (τ) versus shear strain ($d\gamma/dt$) should yield a straight line if the polymer solution or melt behaves like a pseudoplastic liquid. Usually a straight line can be drawn over one to two decades of shear rate, but over a wider range deviations from the Oswald law can be expected."

6.2 Shear thinning in MD simulations

In this work, the following approach to the analysis of the shear viscosity as a function of healing time was adopted. After quenching of the sample from 600 K to 325 K the shear deformation was applied in XY plane along the Y direction parallel to the interface plane of the sample.

The results of the measurements of the shear viscosity η for quenching at 60 ns are shown in Fig. 39. It can be seen from the figure that η has exponential dependence on the shear rate characteristic for shear thinning of the polymers. This result can also be verified by plotting η vs shear rate in the log-log scale as shown in the inset. The latter dependence is linear as expected.

6.3 Time dependence of the interface welding

We now compare the results of measurements of shear viscosity obtained for two different times of welding. The results of comparison of shear viscosity estimated for two different welding times are shown in the Fig. 40.

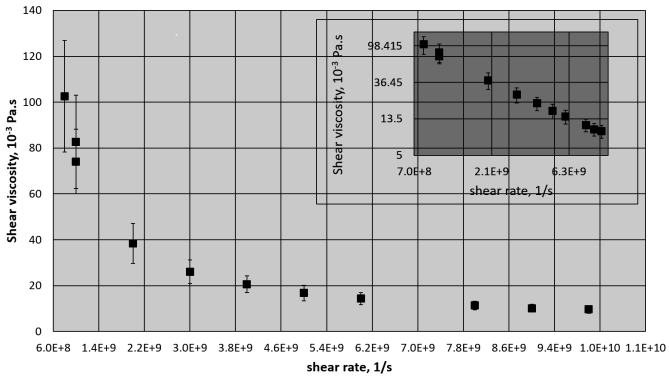

Figure 39: Shear viscosity as a function of shear rate for large system after 60 ns of healing.

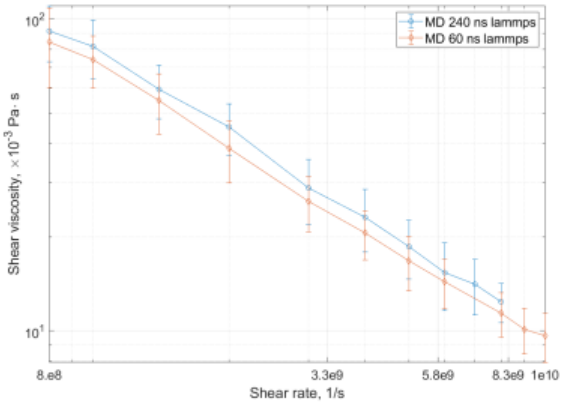

Figure 40: Results of MD estimations of the shear viscosity as a function of the shear rate after quenching at two different welding times.

It can be seen from the figure that the shear viscosity is consistently larger for longer welding time for all shear rates. This result is expected on theoretical grounds, see Sec. 6.1. To validate these results we perform comparison between the values of the shear viscosity obtained in molecular dynamical simulations and experiment.

6.4 Comparison with experimental results

The comparison between experimental results and the results of MD simulations are shown in Fig. 41. The experimental results taken from the site https://www.protolabs.com were obtained for ULTEM 1000 for three different temperatures [67]: (i) 355; (ii) 370 C; and (iii) 385 C. All three temperatures are significantly higher than glass transition temperature. The MD results were obtained for 25 C (significantly below T_g). It is expected that extrapolation of the shear viscosity for small

shear rates should result in larger values than those reported experimentally for $T = 355$ K. At the same time the values of the shear viscosity for ULTEM 9085 are expected to be lower than those obtained for ULTEM 1000. Overall, the comparison of the MD predictions with experimental data obtained for ULTEM 1000 can be considered as a reasonable ballpark estimate.

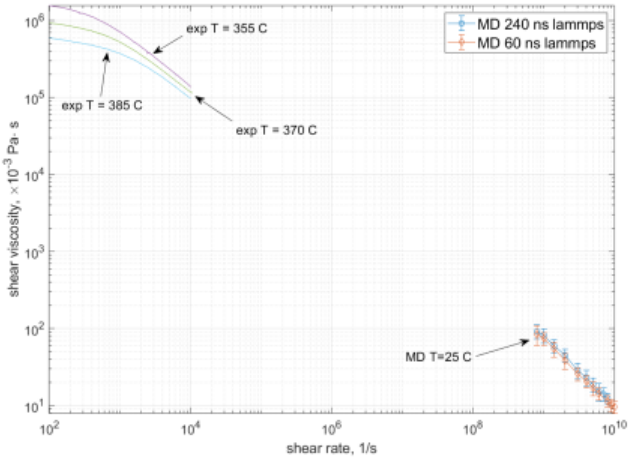

Figure 41: The comparison between the experimental results (upper left corner) and MD simulations (lower right corner). The experimental results taken from the website https://www.protolabs.com were obtained for ULTEM 1000 [67] for 355 C (violet curve), 370 C (green curve), and 385 C (blue curve). The MD results are the same as in the Fig. 40: (i) the shear viscosity obtained after 60ns of welding are shown by open brown diamonds; (ii) the blue open circles correspond to the shear viscosity measured after 240 ns of welding.

It can be seen from the figure that the results of MD simulations are consistent with the experimental results and appear to be on nearly the same shear thinning curve. However, the is a significant gap between the experimental and simulation results. This gap is extending nearly 5 orders of magnitude in the applied shear rates. It prevents more conclusive validation of the MD results.

6.5 Narrowing the gap between the experiment and MD simulations

To narrow the gap we have performed advanced simulations of the shear viscosity using GROMACS and a novel GPU Volta 100 in the Amazon cloud environment. This approach allowed us to extend simulations to 50 ns time (32 cores and one GPU V100) vs 8 ns using LAMMPS (80 cores on supercomputer). Note, however, that GROMACS simulations were using a simple cut-off scheme to calculate the electro-

static interactions and were running for 12 hours for each point on the Amazon cloud. The LAMMPS simulations were using Ewald electrostatics and were running for over two days on supercomputer for each point. Note that the smaller the period of applied deformation, the longer time that is required to run the simulations.

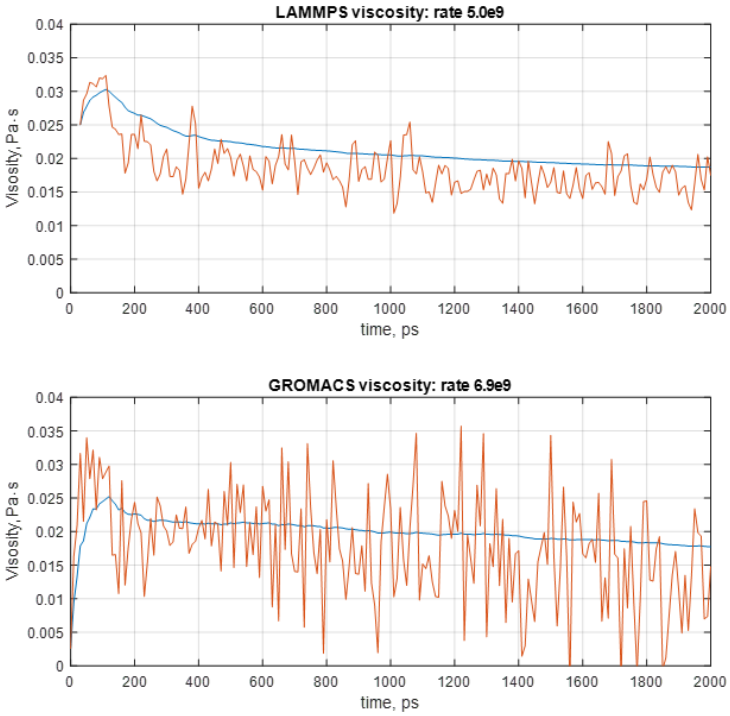

Figure 42: Comparison of the performance of LAMMPS (top pane) and GROMACS (bottom pane) in estimation of the shear viscosity at similar shear rates.

Before extending the simulations to lower rates of deformation we compared performance of GROMACS and LAMMPS. The results of the performance comparison are shown in Fig. 42. It can be noticed that the system response in case of GROMACS and are similar to each other. We therefore used GROMACS in a wider range of deformation rates that strongly overlaps with the earlier results obtained with LAMMPS. The results of the extended simulations are shown in Fig. 43.

It can be seen from the figure that the gap between experiment and MD simulations was reduced from 5 orders of magnitude to less than 2 orders of magnitude. Note that extended comparison between the experiment and MD simulations confirms the general trend mentioned above. Most importantly, it confirms the earlier observation that shear viscosity measured in the experiment and in MD simulations belong to nearly the same shear thinning curve.

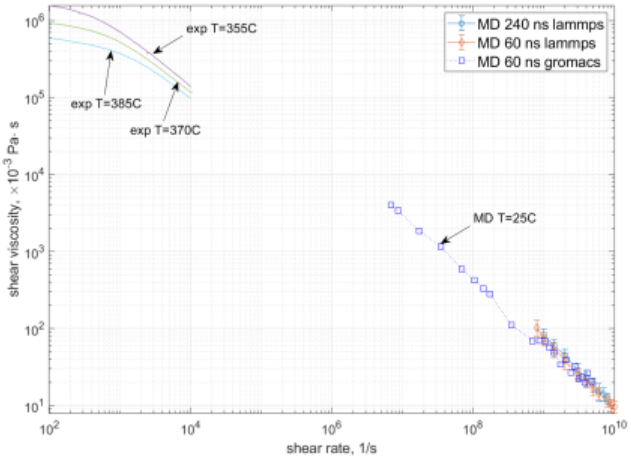

Figure 43: The results of the simulations of the shear viscosity using GROMACS on Amazon cloud (open blue squares) added to the results shown earlier in the Fig. 41.

7 Application

It is known [69] that the fabrication strategy, the envelope temperature of the machine and variations in the convection coefficient have strong effects on the cooling temperature profile, as well as on the mesostructure and overall quality of the bond strength between filaments. In particular, the sintering phenomenon has significant effect on bond formation, but only for the very short duration when the filaments temperature was above the critical sintering temperature. Otherwise, creep deformation was found to dominate changes in the mesostructure.

Therefore we see that there is a trade-off between the strength and deformation of the part that depends mainly on the temperature dynamics at the interface between the bonding filaments. I.e. the longer is the necking process the stronger is the part, but the deformation of the part will also be more pronounced. The resolution of the trade-off requires the separation of the time-scales for necking and reptation at the interface.

In this section we will use results of molecular dynamics simulations to estimate key parameters defining the strength of the parts.

7.1 Reptation time

As was discussed in the previous report one of the key parameters responsible for the strength of the part is the reptation time at the interface. This time provides the characteristic time scale of the interface relaxation to the bulk state. We recall that for a polymer molecule with molecular weight M and repeating unit weight M_0 (the number of

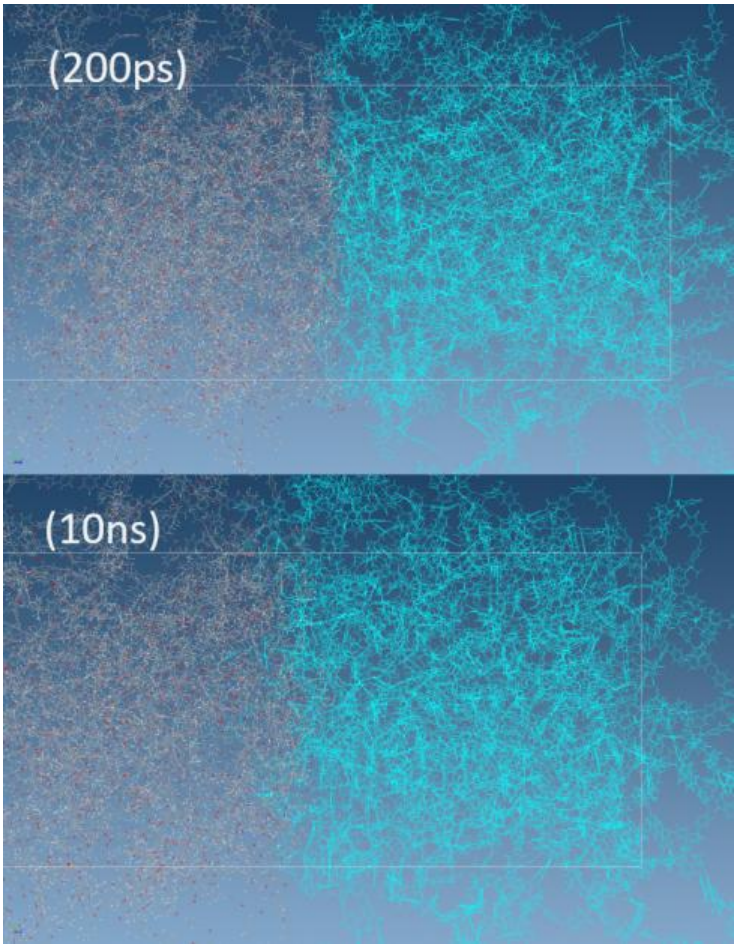

Figure 44: Snapshots of the chain dynamics at the interface during welding. The welding time for each snapshot is shown in the upper right corner.

monomers $N = M/M_0$) the reptation time τ_{rep} can be estimated as [70, 71]

$$\tau_{rep} \simeq R_g^2/D_p \sim M^3 \sim N^3, \tag{12}$$

where R_g and D_p are gyration radius and the self-diffusion coefficient of the melt.

The order of magnitude estimation of the reptation time can be done using results of MD shown in Fig. 44, Fig. 45, and Fig. 46. The maximum chain length that was diffused across the interface is ~ 30 Å. And the average end-to-end distance for polyetherimide chains in our sample is $R \sim 100$ Å, see Fig. 47.

We therefore estimate the reptation time $\tau_{rep} \sim 200ns$. This is consistent with the estimations of the inter-diffusion distance X given by [70, 71]

$$X = R_g(t/\tau_{rep})^{1/4}, \text{ at } t < \tau_{rep}. \tag{13}$$

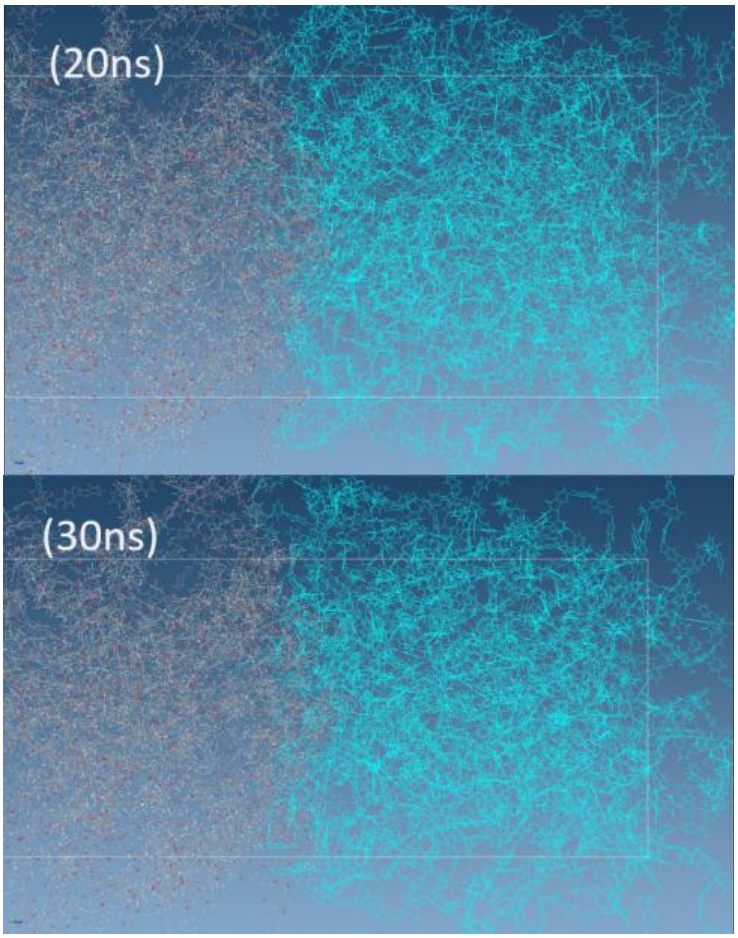

Figure 45: Snapshots of the chain dynamics at the interface during welding. The welding time for each snapshot is shown in the upper right corner (continued from Fig. 44).

X is expected to approach R_g as $t \rightarrow \tau_{rep}$, where $R_g \sim 15$ Å as can be seen from the measurements shown in Fig. 47. The calculated value of X at 240 ns is in agreement with the value obtained from the analysis of the chain dynamics at the interface shown in Fig. 44 - 46.

According to Wool [70], the full strength is obtained when the two polymers filaments are interdiffused at X_∞ equal to 81% of the radius of gyration (R_g), and when further inter-penetration gives the same strength. It follows that our samples approach the full strength at the interface can be reached for our samples in approximately 200 - 400 ns at 600 K.

7.2 Reptation time dependence on degree of polymerization

We note that in our simulations the degree of polymerization of the polymer chains was 5. And in the actual ULTEM 9085 melts the ex-

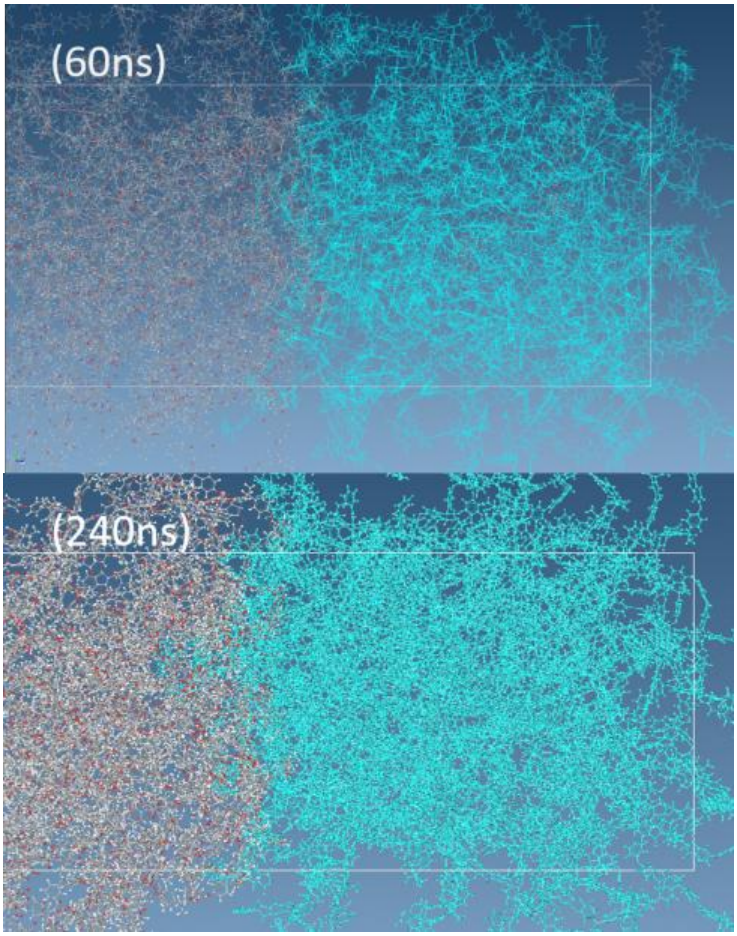

Figure 46: Snapshots of the chain dynamics at the interface during welding. The welding time for each snapshot is shown in the upper right corner (continued from Fig. 45).

pected degree of polymerization is of the order of 70-72. According to the equation (12), the expected value of the reptation time in ULTEM 9085 is of the order of 1 ms for the temperature 600 K.

7.3 Reptation time dependence on the temperature

The above estimations are valid for relatively high temperature 600 K, which is close to the processing temperature during filament deposition.

However, there is strong dependence of the reptation time on the temperature that has to be taken into account. According to Williams-Landel-Ferry (WLF) [72] the reptation time has strong temperature dependence described by the equation

$$\tau_{rep}(T) \sim \tau_e Z^3 a(T), \quad \text{where} \quad a_T(T) = \exp\left(\frac{-C_1(T-T_s)}{C_2+T-T_s}\right), \tag{14}$$

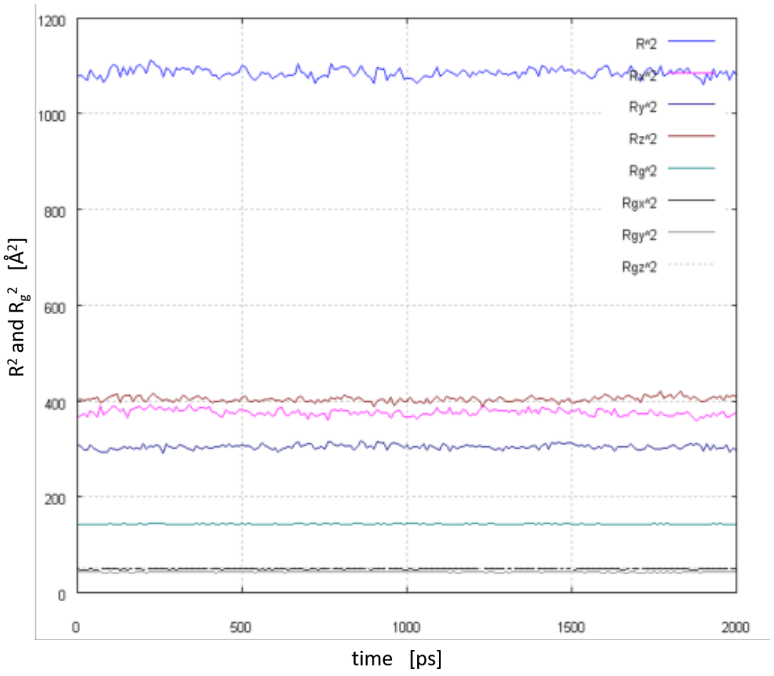

Figure 47: Radius of gyration (R_g) and end-to-end distance (R) of large sample.

where C_1 and C_2 are the constants, τ_e is the equilibration time,which is the Rouse relaxation time of a chain of length equal to one tube segment, T_s is the reference temperature approximately equal to $T_g + 40K$, and Z is the number of reptation tube segments.

To estimate parameters in eq. (14) we use data provided in [72] and add to the original set the recent data of shear viscosity measurements in ULTEM 1000 [67]. The results of fitting of the original data and the new experimental data for zero shear viscosity of ULTEM 1000 (see Fig. 43) is shown in Fig. 48.

To fit the new experimental data to the "universal" $a_T(T)$ curve we use fact that the viscosity is determined by the reptation time [73] and therefore

$$\tau_{rep} \sim \eta \quad \text{and} \quad log(\eta) = \text{const} + \log(a_T(T)).$$

The resulting values of the parameters are as follows: C_1 = 13.12; C_2 = 168.78; T_s = 40. The analysis shows that the exponential growth of the reptation time begins already when the interface temperature $\sim T_s$, i.e. about 40 K above the glass transition temperature. In particular, it follows that the nominal reptation time τ^0_{rep} (i.e. reptation time at $T = T_s$ when $a_T = 1$) is nearly two orders of magnitude larger than the value estimated for T = 600 K. The nominal value of the reptation time can be estimated as $\tau^0_{rep} \sim 100$ ms.

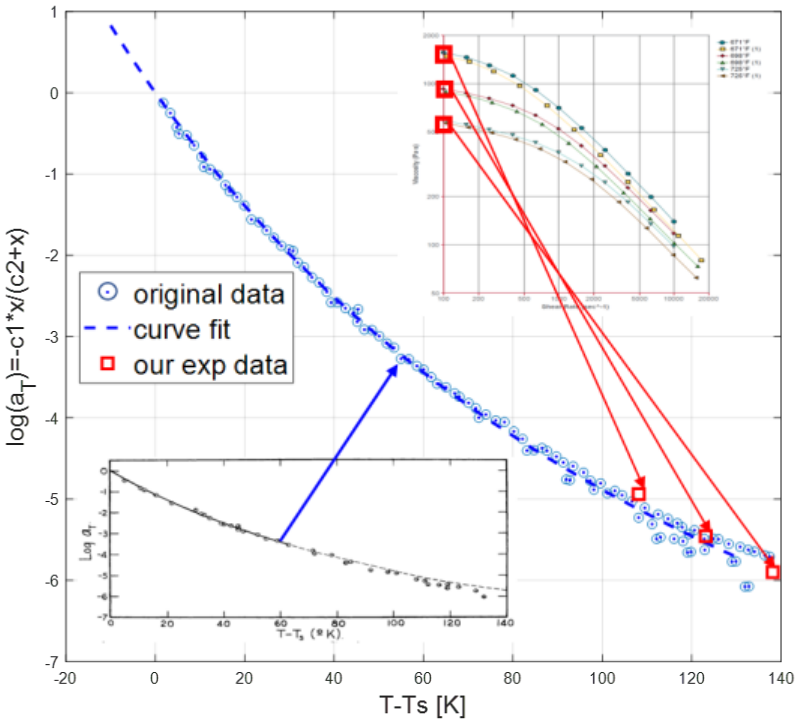

Figure 48: Logarithm of the temperature dependent factor a_T in (14) as a function of $T - T_s$. The original data [72] are shown in the inset in the lower-left corner and by open blue circles with dots in the figure. The fitting curve is shown by the dashed line. The experimental data for viscosity of ULTEM 1000 [67] are shown in the upper-right inset. The zero-shear viscosity points ate shown by red squares. The fit of the zero shear viscosity to the "universal" $a_T(T)$ curve is shown by red squares in the figure.

7.4 Necking dynamics

As was discussed in the beginning of this section the strength of the final part is primarily determined by the size of the neck between two filaments and by the quality of welding of the material at the neck. The time required for material to weld at the interface (the reptation time) was estimated above using results of MD simulations to be of the order of 1 ms at 600 K and can increase up to 100 ms at 530 K. It was also shown that this time is a subject of exponential increasing as the interface is continuing to cool down below T_s.

On the other hand if the characteristic time of necking is of the order of 1 s we still have significant time separation between two characteristic times (welding $\sim$ 100 ms and necking $\sim$ 1 s) as long as the temperature of the interface stays $\geq T_s$ during the sintering process.

We now estimate the characteristic time scale of the necking dynam-

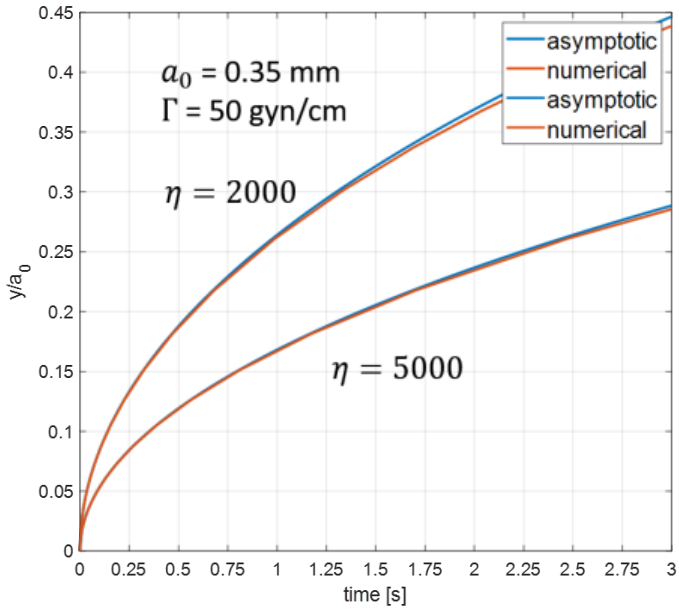

Figure 49: Necking dynamics for two spherical droplets according to modified Frenkel model [74] for two different values of viscosity η 2000 and 5000.

ics at the interface using Frenkel model [74]. By balancing the work of viscous force W_u and work of surface tension W_s

$$W_u = \iiint_V \left[3\eta\dot{\epsilon}^2 dV\right] \quad \text{and} \quad W_s = -\Gamma\frac{dS}{dt}$$

we get the equation for necking dynamics, see Appendix B

$$\theta' = \frac{\Gamma}{a_0\eta}\frac{cos(\theta)sin(\theta)[2-cos(\theta)]^{1/3}}{2^{5/3}[1-cos(\theta)][1+cos(\theta)]^{1/3}} \tag{15}$$

The term $\theta = asin(y/a)$ while a_0, η, and Γ represent the initial particle radius, the viscosity, and the surface tension, respectively. The asymptotic solution is

$$\theta(t) = \left(\frac{t\Gamma}{\eta a_0}\right)^{1/2} \tag{16}$$

It can be seen from the above analysis that the key parameters characterizing time scale of sintering are viscosity and surface tension. Characteristic values of the surface tension for polyetherimide are in the range 38 to 50 dyn/cm. The values of zero shear viscosity can be estimated using results of MD simulations discussed in Sec. 6 to be in the range 2000 to 5000 Pa·s. Using this estimates the dynamics of necking at 600 K can be calculated using the asymptotic expression (16) or by numerical solution of (15).

The results of the corresponding calculations are shown in the Fig. 49. The necking time was estimated in our earlier work to be of the order of 1 sec. It can be seen from the figure that the neck radius approaches $0.15a_0$ at η = 5000 Pa·s and $0.25a_0$ at η = 2000 Pa·s. According to our estimations, the mechanical strength of the interface should approach bulk values at least at the middle of the neck during 1 sec of welding.

We note that the neck radius and the interface strength are exponentially sensitive to the temperature regime. Using typical values of the oven T_o = 170 - 190 C and extruder temperature T_e = 375 - 400 C the problem of trade-off between strength and the deformation of the part can be potentially mitigated. However, a more detailed analysis will be required to establish optimal temperature regime for each specific settings of the manufacturing process that include e.g. deposition velocity, extruder diameter and height, variation in the material properties.

We note also that our analysis shows that the degree of polymerization (DP) of the polymer chains offers another sensitive control parameter over dynamics of the manufacturing process. The DP can often be changed experimentally during ULTEM preparation. Detailed analysis may reveal further possibilities of optimization of the DP, T_b, T_e for given manufacturing settings.

7.5 Extension of the model for the part strength

The obtained results of the molecular dynamical simulations for the shear viscosity allow us to extend our earlier model of the part strength (see Report "Analysis of the mechanical properties of the structures manufactured by fused deposition modeling" [75]) by including effects of viscosity. Indeed, our original model of the part strength is based on the assumption of the elastic response of the polymer blends to the deformation up to the point of yield strength. In particular, the elastic part of the response was modeled as

$$\sigma = E\varepsilon$$

which is valid only for static deformations.

In reality the polymer response to the deformation is viscoelastic. The relation between elastic and viscous types of response strongly depend on the temperature and the rate of deformation. The manufacturing processes and part performance can be characterized by a broad range of the shear deformation rates [76]. For example shear rates for both impact and product performance range from 10^3 to 10^6 1/sec. For such high shear rates significant deviations from the elastic response are expected including both the value of stress and material strength, see Fig. 50

To incorporate these changes into the part strength model developed in our work one can use e.g. KelvinVoigt model to extend the

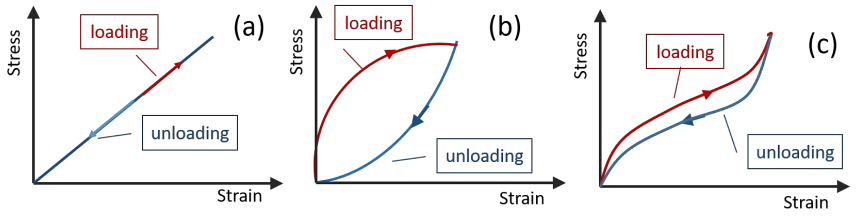

Figure 50: Illustration of the linear elastic behavior with full energy recovery, (b) Non-linear viscoelastic behavior (rate dependent), and (c) viscoplastic behavior.

constitutive equation for the elastic response given above

$$\sigma = E\varepsilon + \eta\dot{\varepsilon}.$$

The latter model accounts for both elastic and viscous response of the material and can be further extended by including shear rate dependence of the shear viscosity $\eta(\dot{\varepsilon})$. Such an extension will be considered in more details in our future work.

8 Conclusions

We developed a novel, fully atomistic approach to MD characterization of welding dynamics at the polymer-polymer interface for blends of amorphous polymers. We applied this approach to the analysis of the welding process at the interface of two amorphous cells of PEI/PC blends. Two systems were considered: small (5,166 atoms) and large (41,328 atoms). The obtained results were then used for molecular dynamical estimations of the key parameters of the system that determined its strength and deformation.

Current state of art. At present, molecular dynamical simulations remain a more expensive, time consuming, and less reliable alternative to the experimental analysis of the properties of the polymer melts. The main value of the MD simulations in this case is statistical estimates of the key parameters of the model that provides a link between the theory and the experiment and an atomistics insight (visual and numerical) into the polymer dynamics. The polymer-polymer interface is one of the most time demanding molecular dynamical simulations because they require large samples for an analysis, where the sample size is determined by the length of the polymer chain.

MD simulations of the interfaces of polymer melts require significant supercomputer power. In earlier research, such simulations were usually limited by the coarse-grained approximations. The coarse- grained approximation does not allow for direct comparison between MD simulations and experiment. In this sense, atomistic MD analysis of the polymer-polymer interface presented in the current report is unique.

Near future expectations. It is expected that the hardware demands of reliable MD predictions regarding properties of the polymer-polymer interfaces can be met within next 5 years under the condition that the GPU technology will continue to grow at a steady rate. It is expected that hardware capabilities will at least double in the near future. Examples include e.g. 5 GHz processors that are expected to be released latter this year and new generation of the graphics cards with GPU support. For example, GTX 2080 Ti was already released and it is claimed to be twice more powerful as compared to GTX 1080 Ti and Volta 100 used in present research. The desktop computers equipped with ~ 24 and more cores with four GTX 2080 Ti are already available for MD simulations.

We expect that larger systems (100,000 atoms and larger) will allow for realistic MD analysis of the thermodynamic and mechanical properties of polymers at the interfaces that can be directly compared to the experiment.

Pilot project. To investigate the prospectives of a cloud computing application to molecular dynamic analysis of polymers, we conducted a pilot project (free of charge) in collaboration with the supercomputing division at Ames and Amazon cloud computing at AWS. During this pilot project we estimated speed and cost of the cloud simulations of our large system. In particular, we calculated the shear viscosity as a function of shear rate that demonstrates shear thinning behavior of our polymer models and allows for direct comparison with the experiment. The results of our pilot project indicate that very large systems (over 100,000 atoms) can be efficiently analyzed using GPU based cloud computing. The cloud based systems remain pricey and the dynamics of the market of cloud computing is hard to predict.

Main conclusions

The focus of the present research was to provide molecular dynamics estimations of the key parameters affecting welding at the filament interfaces and the strength of the manufactured parts. To validate the results of MD simulations we used experimentally measured infra-red spectra, glass transition temperature, and specific heat capacity. At the first step of validation we calculated vibrational and infrared spectra of the amorphous sample for four different force fields DREIDING, GAFF, OPLS-AA, and OPLS-AA with quantum corrections. It was shown that a good agreement with the experimental data can be obtained using OPLS-AA force field with quantum corrections.

At the second step of validation we compared MD predictions with experimental data for the following thermo-mechanical parameters:

- density of the sample;
- glass transition temperature;
- bulk modulus as a function of time;

- coefficient of volumetric thermal expansion as a function of time;
- heat capacity as a function of time.

Despite some discrepancies we consider the results of the validation satisfactory. We believe that obtained results shown convincingly that the proposed method of fully atomistic modeling of polymer-polymer interfaces allows for quantitative estimations of the important thermo-mechanical parameters. The difficulties remain though in estimations of the jump of the heat capacity at the glass transition.

After the validation we used molecular dynamical simulations to estimate

- bulk modulus;
- coefficient of thermal expansion;
- Young modulus;
- the shear viscosity as a function of shear rate of ULTEM 9085;
- reptation time at the interface;
- thickness of the welded layer at the interface;
- necking dynamics.

The bulk modulus of the amorphous PEI/PC blends was estimated for small and large system. The bulk modulus as a function of temperature of a small sample was estimated using "direct" MD measurements of the volume change as a function of pressure for different temperatures. For a large sample, the bulk modulus was estimated using fluctuations. It was shown that after 15 ns of integration time the fluctuation based method converged to the results obtained by direct measurements. The estimated values of the bulk modulus are in reasonable agreement with experimental data and results of earlier MD simulations in similar materials [41].

The estimated values and the general trend of the temperature dependence of the coefficient of thermal expansion also follow the expected behavior. The values of the α_P are in agreement with earlier MD estimations in similar materials [41].

The most difficult measurements of the present research was estimation of the shear viscosity as a function of the shear rate in the samples with polymer-polymer interface. The majority of earlier research was based on the coarse-grained approximation that does not allow for direct comparison with the experiment. In the present research, we performed unique fully atomistic modeling of such interfaces. The main difficulty of our approach was the long integration time required to calculate shear viscosity for the shear rate less than 10^7 1/sec. To perform such calculations we used amazon cloud services enhanced with GPU capabilities.

The obtained results

- clearly reveal the shear thinning behavior of the shear viscosity as a function of shear rate;
- demonstrate the dependence of the shear viscosity on the welding time and to show that at the welding temperature 600 K the shear viscosity begin to approach the bulk value after ∼ 240 ns of welding;
- perform direct comparison with experimental data.

A good agreement between values of shear viscosity estimated in MD simulations and experimental data was demonstrated. Importantly, by using GPU based nodes on Amazon cloud AWS we narrowed the gap between computed and measured data by over two orders of magnitude: from 5-orders to 2 and half orders of magnitude.

Overall, the comparison of MD predictions with experimental data suggest that a reasonable agreement between experiment and MD simulations can be achieved for the sample size larger than 40,000 atoms. We expect significant improvement of the MD predicted values with the size of the sample of the order 100,000 atoms and integration time ∼ 25 ns. Our analysis also provides evidence that the hardware and software development will enable more accurate MD predictions of polymer properties at reasonable price in the near future.

The results of MD simulations were used to estimate one of the key parameters that determine the strength of the part - the reptation time at the interface. The value of τ_{rept} at the interface was estimated as ∼ 1 ms for 600 K. We have also estimated the dependence of this time on the welding temperature. It was shown that the reptation time is very sensitive (exponential) to the changes of the welding temperature and can be of the order of 100 ms at $T_{interface}$ 40 K above the glass transition temperature.

The results of the MD measurements of the shear viscosity were used to estimate the dynamics of necking (sintering) at the interface between two filaments. In our work (see Report "Analysis of the mechanical properties of the structures manufactured by fused deposition modeling" [75]) we showed that the sintering takes place on the time scale ∼1 s. During this time the neck growth depends significantly on the oven and extruder temperatures and on the viscosity of the sample. Calculations show that during 1 s of sintering time the neck radius approaches the value ∼0.25 a_0 for $\eta = 2000 Pa \cdot s$ and the value ∼0.15 a_0 for $\eta = 5000 Pa \cdot s$.

Using these estimations we discussed the trade-off between strength and the deformation of the part. We notice that although standard oven (T_o ∼ 170 - 190C) and extruder (T_e ∼ 375 - 400C) temperatures are potentially suitable for mitigation of the trade-off problem a further fine tuning of their values may be required for each specific manufacturing process. Such tuning may become important because of the exponential

sensitivity of the strength with respect to the changes of these parameters. It was suggested that the degree of polymerization of the polymer chains can be potentially used as an additional sensitive control parameter of the process.

We used MD measurements of the strain-stress curve during elongation of large sample to support development of the part strength model proposed in our work, see Report "Analysis of the mechanical properties of the structures manufactured by fused deposition modeling" [75]. Furthermore, our MD measurements of the shear stress as a function of shear rate were used to propose an extension of this model by using Kelvin-Voigt model of viscoelasticity. Such an extension will incorporate the dependence to the part deformation on the rate of sample loading and unloading and will be considered in more details in the future work.

Appendices

Appendix A

Experimental data sets

In this project we use two sets of experimental data. The first set was provided by the MSFC group and includes infrared absorbance spectra and specific heat capacity for ULTEM 9085. The experimental absorbance spectra and specific heat capacity are shown in Fig. A.1.

The second set of data was provided by Prospector LLC and includes results of the following properties measured for ULTEM 1000 [29]: (i) density; (ii) bulk modulus ; (iii) coefficient of linear thermal expansion; (iv) specific heat capacity (with (i) to (iv) measured as functions of temperature); (v) viscosity as a function of shear rate; and (iv) stress as a function of strain.

The experimental data for ULTEM 1000 are shown in Fig. A.2.

Appendix B

Frenkel's model of sintering [74]

We consider a coalescence of two polymer droplets by taking into account tension forces and dissipation.

Under assumption of constant mass and if density of the polymers

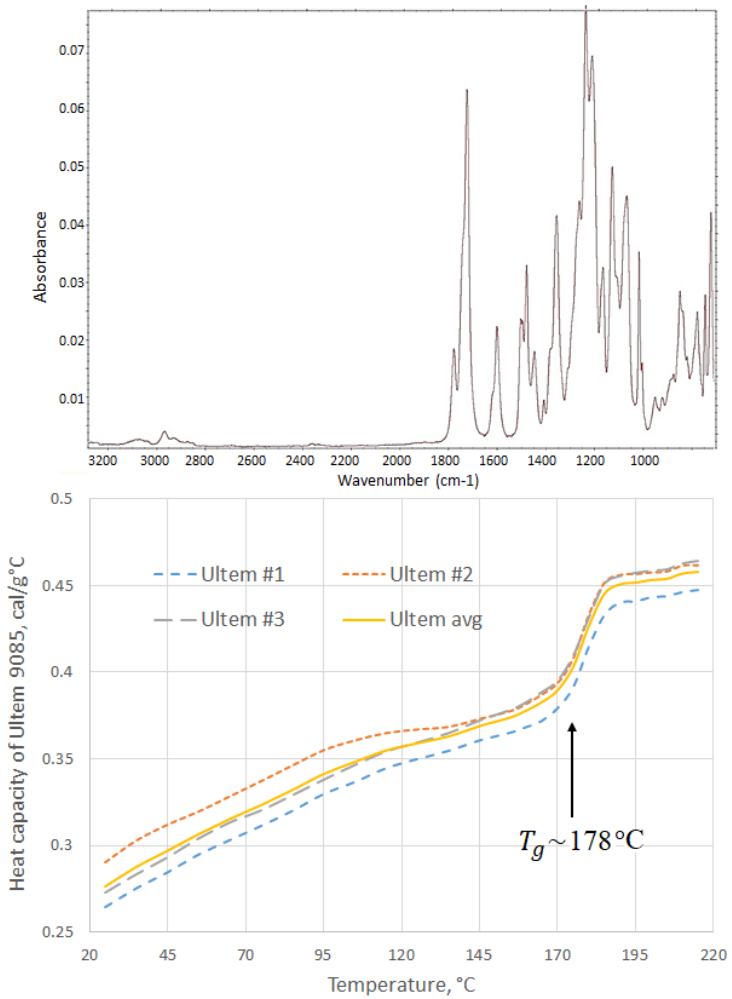

Figure A.1: Experimental data provided by MSFC for ULTEM 9085. (left) Infrared absorbance spectra and (right) specific heat capacity as a function of temperature.

the following relation between $\theta(t)$ and $a(t)$ is valid at all times

$$a(t) = a_0\left(\frac{4}{(1+\cos\theta(t))^2(2-\cos\theta(t))}\right)^{1/3} \tag{B.2}$$

The area of the curved surface is

$$S = 4\pi a^2(t)(1+\cos\theta(t)) \tag{B.2}$$

The work of viscous forces W_v for Newtonian fluids is[4]

$$W_u = \iiint_V \eta\nabla u : \left(\nabla u + \nabla u^T\right) dV \tag{B.2}$$

[4]The double dot (or scalar, or inner) product produces a scalar

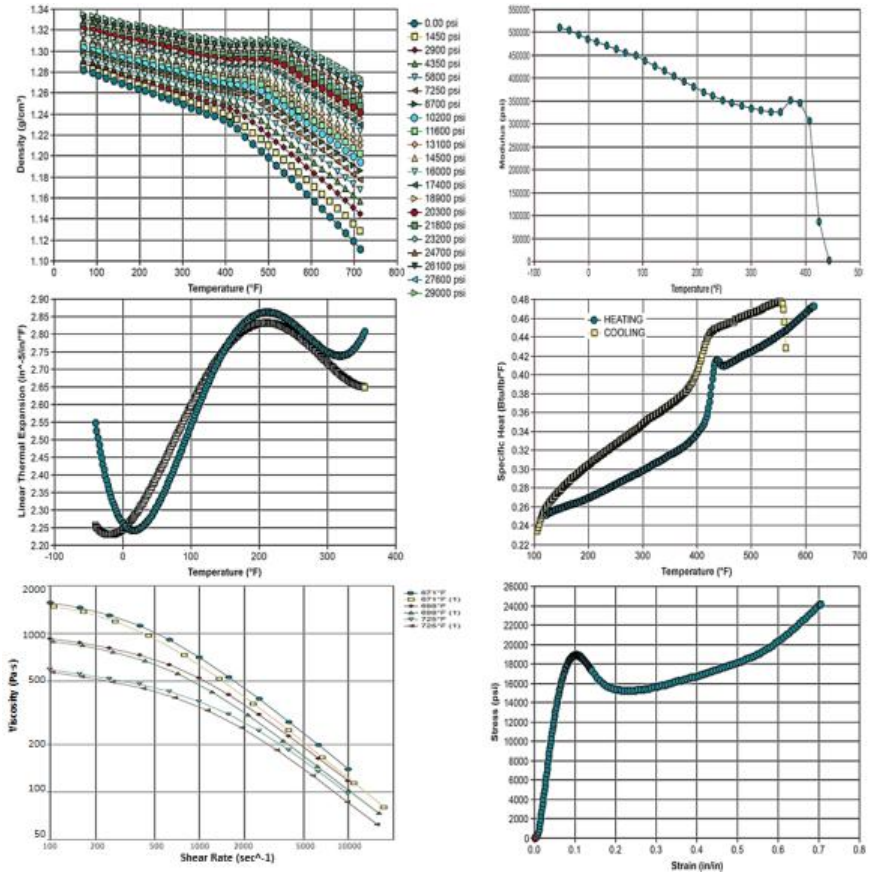

Figure A.2: The set of data provided by Prospector LLC for ULTEM 1000 [29]: (i) density; (ii) bulk modulus ; (iii) coefficient of linear thermal expansion; (iv) specific heat capacity (with (i) to (iv) measured as functions of temperature); (v) viscosity as a function of shear rate; and (iv) stress as a function of strain.

where

$$\nabla u = \begin{bmatrix} \frac{\dot{\epsilon}}{2} & 0 & 0 \\ 0 & -\dot{\epsilon} & 0 \\ 0 & 0 & \frac{\dot{\epsilon}}{2} \end{bmatrix}.$$

The resulting expression for the viscous force is

$$W_u = \iiint_V 3\eta\dot{\epsilon}^2 dV, \tag{B.2}$$

where

$$\dot{\epsilon} = \frac{\partial u_y(A)}{\partial y} = \frac{u_y(A) - u_y(O)}{a}$$

and $u_y(A)$ is the velocity with which point A moves towards point O and $u_y(O) = 0$.

The resulting equations for $u_y(A)$ and $\dot{\epsilon}$ are

$$u_y(A) = -\frac{a_0 2^{5/3}\sin(\theta)}{[1+\cos(\theta)]^{5/3}[2-\cos(\theta)]^{4/3}}\theta', \qquad \dot{\epsilon} = \frac{u_y(A)}{a} = -\frac{2\sin(\theta)}{[1+\cos(\theta)][2-\cos(\theta)]}\theta' \tag{B.2}$$

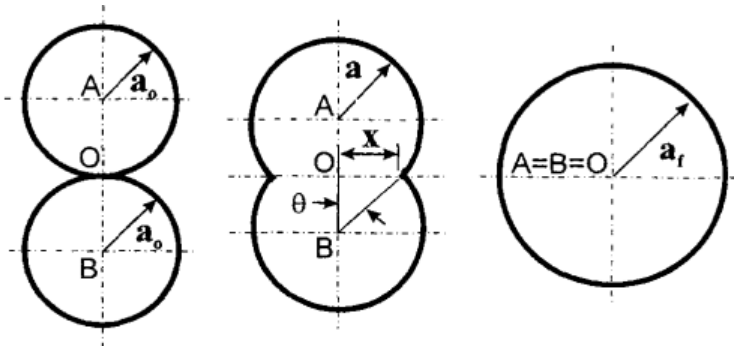

Figure B.3: Shape evolution in Frenkel's model [74]

Substituting these results into (B.2) and taking into account the fact the the volume of the two droplets does not change we have

$$W_v = 32\pi a_0^3 \eta \frac{1-\cos(\theta)}{[1+\cos(\theta)][2-\cos(\theta)]^2}(\theta')^2 \tag{B.3}$$

The energy dissipated in unit W_u time during spreading has to be equated to the change of the energy due to work of the surface tension W_s

$$W_s = -\Gamma\frac{dS}{dt} = \Gamma\frac{8\pi a_0^2 2^{1/3}\cos(\theta)\sin(\theta)}{[1+\cos(\theta)]^{4/3}[2-\cos(\theta)]^{5/3}}\theta' \tag{B.3}$$

By equating (B.3) and (B.3) we obtain equation for the neck angle dynamics

$$\theta' = \frac{\Gamma}{a_0\eta}\frac{\cos(\theta)\sin(\theta)[2-\cos(\theta)]^{1/3}}{2^{5/3}[1-\cos(\theta)][1+\cos(\theta)]^{1/3}} \tag{B.3}$$

This expression is singular at $t = 0$. To avoid singularity asymptotic solution is obtained asymptotic solution is obtained for small t by expanding the right hand side at $t = 0$. The equation with the expanded right hand side is

$$\theta' = \frac{1}{2}\frac{\Gamma}{\eta a_0 \theta} \tag{B.3}$$

with solution given by

$$\theta(t) = \left(\frac{t\Gamma}{\eta a_0}\right)^{1/2}. \tag{B.3}$$

Accordingly, the initial conditions for mention of equation (B.3) are provided at small finite t using values obtained using asymptotic formula (B.3).

References

1. B. Bhushan, Springer Handbook of Nanotechnology (Springer Handbooks), Springer, 2017. doi:10.1007/978-3-642-02525-9.

2. J. D. Monk, J. B. Haskins, C. W. Bauschlicher, J. W. Lawson, Molecular dynamics simulations of phenolic resin: Construction of atomistic models, Polymer 62 (2015) 39–49. doi:10.1016/j.polymer.2015.02.003.

3. S. G. Falkovich, S. V. Lyulin, V. M. Nazarychev, S. V. Larin, A. A. Gurtovenko, N. V. Lukasheva, A. V. Lyulin, Influence of the electrostatic interactions on thermophysical properties of polyimides: Molecular-dynamics simulations, Journal of Polymer Science Part B: Polymer Physics 52 (9) (2014) 640–646. doi:10.1002/polb.23460.

4. X. He, Y. Zhu, Y. Mo, Origin of fast ion diffusion in super-ionic conductors, Nature Communications 8 (2017) 15893. doi:10.1038/ncomms15893.

5. S. Majd, E. C. Yusko, Y. N. Billeh, M. X. Macrae, J. Yang, M. Mayer, Applications of biological pores in nanomedicine, sensing, and nanoelectronics, Current opinion in biotechnology 21 (4) (2010) 439–476.

6. M. Ali, B. Yameen, R. Neumann, W. Ensinger, W. Knoll, O. Azzaroni, Biosensing and supramolecular bioconjugation in single conical polymer nanochannels. facile incorporation of biorecognition elements into nanoconfined geometries, Journal of the American Chemical Society 130 (48) (2008) 16351–16357, pMID: 19006302. arXiv:http://dx.doi.org/10.1021/ja8071258.

7. Z. Xu, I. Michos, Z. Cao, W. Jing, X. Gu, K. Hinkle, S. Murad, J. Dong, Proton-selective ion transport in zsm-5 zeolite membrane, The Journal of Physical Chemistry C 120 (46) (2016) 26386–26392. arXiv:http://dx.doi.org/10.1021/acs.jpcc.6b09383.

8. B. Logan, M. Elimelech, Membrane-based processes for sustainable power generation using water 488 (2012) 313–9.

9. B. E. Eichinger, D. Rigby, J. Stein, Cohesive properties of Ultem and related molecules from simulations, Polymer 43 (2) (2002) 599–607.

10. R. Zhang, W. L. Mattice, Flexibility of a new thermoplastic polyimide studied with molecular simulations, Macromolecules 26 (22) (1993) 6100–6105. doi:10.1021/ma00074a035.

11. S. V. Lyulin, S. V. Larin, A. A. Gurtovenko, N. V. Lukasheva, V. E. Yudin, V. M. Svetlichnyi, A. V. Lyulin, Effect of the SO2 group in the diamine fragment of polyimides on their structural, thermophysical, and mechanical properties, Polymer Science Series A 54 (8) (2012) 631–643. doi:10.1134/s0965545x12070048.

12. S. V. Lyulin, A. A. Gurtovenko, S. V. Larin, V. M. Nazarychev, A. V. Lyulin, Microsecond atomic-scale molecular dynamics simulations of polyimides, Macromolecules 46 (15) (2013) 6357–6363. arXiv:http://dx.doi.org/10.1021/ma4011632, doi:10.1021/ma4011632.
URL http://dx.doi.org/10.1021/ma4011632

13. V. M. Nazarychev, A. Y. Dobrovskiy, S. V. Larin, A. V. Lyulin, S. V. Lyulin, Simulating local mobility and mechanical properties of thermostable polyimides with different dianhydride fragments, Journal of Polymer Science Part B: Polymer Physics 56 (5) (2017) 375–382. doi:10.1002/polb.24550.

14. A. de Nicola, A. Correa, G. Milano, P. L. Manna, P. Musto, G. Mensitieri, G. Scherillo, Local structure and dynamics of water absorbed in poly(ether imide): A hydrogen bonding anatomy, The Journal of Physical Chemistry B 121 (14) (2017) 3162–3176. doi:10.1021/acs.jpcb.7b00992.

15. J. Ramiro, J. I. Eguiazábal, J. Nazábal, Phase structure and mechanical properties of blends of poly(ether imide) and bisphenol a polycarbonate, Polymer Journal 36 (9) (2004) 705–715. doi:10.1295/polymj.36.705.

16. P. Bajaj, D. Bajaj, C. Strom, H. Zhou, K. Leung, Understanding the structure-process-property balance in pc/pei blends by morphology (using scanning transmission electron microscopy in field emission -scanning electron microscopy) and correlative deformation mechanics 21 (2015) 613–614.

17. M. Zhang, P. Choi, U. Sundararaj, Molecular dynamics and thermal analysis study of anomalous thermodynamic behavior of poly (ether imide)/polycarbonate blends, Polymer 44 (6) (2003) 1979–1986.

18. F. Pierce, D. Perahia, G. S. Grest, Dynamics of polymers across an interface, EPL (Europhysics Letters) 95 (4) (2011) 46001.

19. K. Yokomizo, Y. Banno, M. Kotaki, Molecular dynamics study on the effect of molecular orientation on polymer welding, Polymer 53 (19) (2012) 4280–4286. doi:10.1016/j.polymer.2012.07.042.

20. T. Ge, G. S. Grest, M. O. Robbins, Structure and strength at immiscible polymer interfaces, ACS Macro Letters 2 (10) (2013) 882–886. arXiv:http://dx.doi.org/10.1021/mz400407m.

21. T. Ge, M. O. Robbins, D. Perahia, G. S. Grest, Healing of polymer interfaces: Interfacial dynamics, entanglements, and strength, Phys. Rev. E 90 (2014) 012602.

22. M. Bulacu, E. van der Giessen, Effect of bending and torsion rigidity on self-diffusion in polymer melts: A molecular-dynamics study, The Journal of Chemical Physics 123 (11) (2005) 114901. doi:10.1063/1.2035086.

23. A. Chremos, C. Jeong, J. F. Douglas, Influence of polymer architectures on diffusion in unentangled polymer melts, Soft Matter 13 (34) (2017) 5778–5784. doi:10.1039/c7sm01018d.

24. J. Gardan, Additive manufacturing technologies: state of the art and trends, International Journal of Production Research 54 (10) (2015) 3118–3132. doi:10.1080/00207543.2015.1115909.

25. G. Cicala, G. Ognibene, S. Portuesi, I. Blanco, M. Rapisarda, E. Pergolizzi, G. Recca, Comparison of ultem 9085 used in fused deposition modelling (FDM) with polytherimide blends, Materials 11 (2) (2018) 285. doi:10.3390/ma11020285.

26. R. Zaldivar, D. Witkin, T. McLouth, D. Patel, K. Schmitt, J. Nokes, Influence of processing and orientation print effects on the mechanical and thermal behavior of 3d-printed ULTEM ® 9085 material, Additive Manufacturing 13 (2017) 71–80. doi:10.1016/j.addma.2016.11.007.

27. K. P. Motaparti, G. Taylor, M. C. Leu, K. Chandrashekhara, J. Castle, M. Matlack, Experimental investigation of effects of build parameters on flexural properties in fused deposition modelling parts, Virtual and Physical Prototyping 12 (3) (2017) 207–220. doi:10.1080/17452759.2017.1314117.

28. C. McIlroy, P. D. Olmsted, Deformation of an amorphous polymer during the fused-filament-fabrication method for additive manufacturing, Journal of Rheology 61 (2) (2017) 379–397. doi:10.1122/1.4976839.

29. L. ULProspector.com from UL, Heat capacity, https://www.protolabs.com/media/1014801/ultem-1000-im.pdf (2018).

30. S. L. Mayo, B. D. Olafson, W. A. Goddard, Dreiding: a generic force field for molecular simulations, The Journal of Physical Chemistry 94 (26) (1990) 8897–8909. arXiv:http://dx.doi.org/10.1021/j100389a010.

31. JSOL corp., User's Manual, J-OCTA Overview, J-OCTA 4.0 (2018). URL http://www.j-octa.com/

32. M. W. Schmidt, K. K. Baldridge, J. A. Boatz, S. T. Elbert, M. S. Gordon, J. H. Jensen, S. Koseki, N. Matsunaga, K. A. Nguyen, S. Su, T. L. Windus, M. Dupuis, J. A. Montgomery, General atomic and molecular electronic structure system, Journal of Computational Chemistry 14 (11) (1993) 1347–1363. doi:10.1002/jcc.540141112.

33. M. S. Gordon, M. W. Schmidt, Advances in electronic structure theory, in: Theory and Applications of Computational Chemistry, Elsevier, 2005, pp. 1167–1189. doi:10.1016/b978-044451719-7/50084-6.

34. S. Plimpton, Fast parallel algorithms for short-range molecular dynamics, Tech. rep. (may 1993). doi:10.2172/10176421.

35. T. W. Sirk, S. Moore, E. F. Brown, Characteristics of thermal conductivity in classical water models, The Journal of Chemical Physics 138 (6) (2013) 064505. doi:10.1063/1.4789961.

36. H. Berendsen, D. van der Spoel, R. van Drunen, GROMACS: A message-passing parallel molecular dynamics implementation, Computer Physics Communications 91 (1-3) (1995) 43–56. doi:10.1016/0010-4655(95)00042-e.

37. E. Lindahl, B. Hess, D. van der Spoel, GROMACS 3.0: a package for molecular simulation and trajectory analysis, Journal of Molecular Modeling 7 (8) (2001) 306–317. doi:10.1007/s008940100045.

38. S. Pronk, S. Páll, R. Schulz, P. Larsson, P. Bjelkmar, R. Apostolov, M. R. Shirts, J. C. Smith, P. M. Kasson, D. van der Spoel, B. Hess, E. Lindahl, GROMACS 4.5: a high-throughput and highly parallel open source molecular simulation toolkit, Bioinformatics 29 (7) (2013) 845–854. doi:10.1093/bioinformatics/btt055.

39. M. J. Abraham, T. Murtola, R. Schulz, S. Páll, J. C. Smith, B. Hess, E. Lindahl, GROMACS: High performance molecular simulations through multi-level parallelism from laptops to supercomputers, SoftwareX 1-2 (2015) 19–25. doi:10.1016/j.softx.2015.06.001.

40. S. Páll, M. J. Abraham, C. Kutzner, B. Hess, E. Lindahl, Tackling exascale software challenges in molecular dynamics simulations with GROMACS, in: Lecture Notes in Computer Science, Springer International Publishing, 2015, pp. 3–27. doi:10.1007/978-3-319-15976-8_1.

41. C. Li, G. A. Medvedev, E.-W. Lee, J. Kim, J. M. Caruthers, A. Strachan, Molecular dynamics simulations and experimental studies

of the thermomechanical response of an epoxy thermoset polymer, Polymer 53 (19) (2012) 4222–4230. doi:10.1016/j.polymer.2012.07.026.

42. I. N. Levine, Quantum Chemistry, Prentice Hall College Div, 1991.

43. C. Møller, M. S. Plesset, Note on an approximation treatment for many-electron systems, Physical Review 46 (7) (1934) 618–622. doi:10.1103/physrev.46.618.

44. G. D. Purvis, R. J. Bartlett, A full coupled-cluster singles and doubles model: The inclusion of disconnected triples, The Journal of Chemical Physics 76 (4) (1982) 1910–1918. doi:10.1063/1.443164.

45. K. Raghavachari, G. W. Trucks, J. A. Pople, M. Head-Gordon, A fifth-order perturbation comparison of electron correlation theories, Chemical Physics Letters 157 (6) (1989) 479–483. doi:10.1016/s0009-2614(89)87395-6.

46. R. Ditchfield, W. J. Hehre, J. A. Pople, Self-consistent molecular-orbital methods. IX. an extended gaussian-type basis for molecular-orbital studies of organic molecules, The Journal of Chemical Physics 54 (2) (1971) 724–728. doi:10.1063/1.1674902.

47. P. J. Flory, Statistical Mechanics of Chain Molecules, Interscience, 1969.

48. K. Trachenko, V. V. Brazhkin, Heat capacity at the glass transition, Physical Review B 83 (1). doi:10.1103/physrevb.83.014201.

49. K. Trachenko, V. V. Brazhkin, Collective modes and thermodynamics of the liquid state, Reports on Progress in Physics 79 (1) (2015) 016502. doi:10.1088/0034-4885/79/1/016502.

50. M. P. Allen, D. J. Tildesley, Computer Simulation of Liquids (Oxford Science Publications), Clarendon Press, 1989.

51. Q. Wang, D. J. Keffer, S. Petrovan, J. B. Thomas, Molecular dynamics simulation of poly(ethylene terephthalate) oligomers, The Journal of Physical Chemistry B 114 (2) (2010) 786–795. doi:10.1021/jp909762j.

52. P. H. Berens, D. H. J. Mackay, G. M. White, K. R. Wilson, Thermodynamics and quantum corrections from molecular dynamics for liquid water, The Journal of Chemical Physics 79 (5) (1983) 2375–2389. doi:10.1063/1.446044.

53. P. Mott, J. Dorgan, C. Roland, The bulk modulus and poisson's ratio of “incompressible” materials, Journal of Sound and Vibration 312 (4-5) (2008) 572–575. doi:10.1016/j.jsv.2008.01.026.

54. M. Doi, S. Edwards, The Theory of Polymer Dynamics, International series of monographs on physics, Clarendon Press, 1988.

55. T. Ge, F. Pierce, D. Perahia, G. S. Grest, M. O. Robbins, Molecular dynamics simulations of polymer welding: Strength from interfacial entanglements, Physical Review Letters 110 (9). doi:10.1103/physrevlett.110.098301.

56. J.-M. Y. Carrillo, S. Cheng, R. Kumar, M. Goswami, A. P. Sokolov, B. G. Sumpter, Untangling the effects of chain rigidity on the structure and dynamics of strongly adsorbed polymer melts, Macromolecules 48 (12) (2015) 4207–4219. doi:10.1021/acs.macromol.5b00624.

57. A. V. Dobrynin, Electrostatic persistence length of semiflexible and flexible polyelectrolytes, Macromolecules 38 (22) (2005) 9304–9314. doi:10.1021/ma051353r.

58. S. Voiutskii, Autohesion and adhesion of high polymers, Polymer reviews, Wiley, 1963.
URL https://books.google.com/books?id=DLY8AAAAIAAJ

59. S. Prager, M. Tirrell, The healing process at polymer-polymer interfaces, The Journal of Chemical Physics 75 (10) (1981) 5194–5198. doi:10.1063/1.441871.

60. Y. H. Kim, R. P. Wool, A theory of healing at a polymer-polymer interface, Macromolecules 16 (7) (1983) 1115–1120. arXiv:http://dx.doi.org/10.1021/ma00241a013.

61. R. H. Ewell, H. Eyring, Theory of the viscosity of liquids as a function of temperature and pressure, The Journal of Chemical Physics 5 (9) (1937) 726–736. doi:10.1063/1.1750108.

62. M. Joly, Non-newtonian surface viscosity, Journal of Colloid Science 11 (4-5) (1956) 519–531. doi:10.1016/0095-8522(56)90168-4.

63. L. Landau, E. Lifshitz, A. Kosevich, J. Sykes, L. Pitaevskii, W. Reid, Theory of Elasticity, Course of theoretical physics, Elsevier Science, 1986.
URL https://books.google.com/books?id=tpY-VkwCkAIC

64. J. H. Irving, J. G. Kirkwood, The statistical mechanical theory of transport processes. IV. the equations of hydrodynamics, The Journal of Chemical Physics 18 (6) (1950) 817–829. doi:10.1063/1.1747782.

65. C. Gray, C. Gray, K. Gubbins, C. Joslin, C. G, Theory of Molecular Fluids: I: Fundamentals, International Series of Monogr, OUP Oxford, 1984.
URL https://books.google.co.uk/books?id=3mz2RcnnMGwC

66. T. Aoyagi, Coarse-grained molecular dynamics study of the interface of polymer blends, Nihon Reoroji Gakkaishi 37 (2) (2009) 75–79. doi:10.1678/rheology.37.75.

67. S. Ltd, Ultem 9085 (2019).
URL https://www.stratasys.com/materials/search/ultem9085

68. P. P. Database, Flow properties of polymers (2015).
URL http://polymerdatabase.com/polymer%20physics/Viscosity2.html

69. Q. Sun, G. Rizvi, C. Bellehumeur, P. Gu, Effect of processing conditions on the bonding quality of FDM polymer filaments, Rapid Prototyping Journal 14 (2) (2008) 72–80.

70. R. Wool, Polymer Interfaces: Structure and Strength, Hanser Publishers, 1995.

71. R. P. Wool, K. M. O'Connor, Time dependence of crack healing, Journal of Polymer Science: Polymer Letters Edition 20 (1) (1982) 7–16.

72. M. L. Williams, R. F. Landel, J. D. Ferry, The temperature dependence of relaxation mechanisms in amorphous polymers and other glass-forming liquids, Journal of the American Chemical Society 77 (14) (1955) 3701–3707. doi:10.1021/ja01619a008.

73. P. de Gennes, Scaling Concepts in Polymer Physics, Cornell University Press, 1979.

74. O. Pokluda, C. T. Bellehumeur, J. Vlachopoulos, Modification of Frenkel's model for sintering, AIChE Journal 43 (12) (1997) 3253–3256.

75. D. G. L. K. R. W. V. Hafiychuk, H. Hafiychuk, Analysis of the mechanical properties of the structures manufactured by fused deposition modeling, Technical Publication NASA/TP-2019 to be published, NASA, ARC (2019).

76. W. Cox, E. Merz, Understanding rheology of thermoplastic polymers, 2013.

REPORT DOCUMENTATION PAGE

Form Approved
OMB No. 0704–0188

1. REPORT DATE *(DD-MM-YYYY)*	2. REPORT TYPE	3. DATES COVERED *(From - To)*
01-12-2018	Technical Memorandum	03/2017–11/2018

4. TITLE AND SUBTITLE
Molecular dynamics of ULTEM 9085 for 3D manufacturing: spectra, thermodynamic properties, and shear viscosity.

5a. CONTRACT NUMBER

5b. GRANT NUMBER

5c. PROGRAM ELEMENT NUMBER

6. AUTHOR(S)
Dmitry G. Luchinsky, Halina Hafiychuk, Vasyl Hafiychuk, Kevin R. Wheeler

5d. PROJECT NUMBER

5e. TASK NUMBER
00370.04C.212.001

5f. WORK UNIT NUMBER

7. PERFORMING ORGANIZATION NAME(S) AND ADDRESS(ES)
NASA Ames Research Center
Moffett Field, California 94035-2199

8. PERFORMING ORGANIZATION REPORT NUMBER
L–12456

9. SPONSORING/MONITORING AGENCY NAME(S) AND ADDRESS(ES)
National Aeronautics and Space Administration
Washington, DC 20546-0001

10. SPONSOR/MONITOR'S ACRONYM(S)
NASA

11. SPONSOR/MONITOR'S REPORT NUMBER(S)
NASA/TM–2018–220213

12. DISTRIBUTION/AVAILABILITY STATEMENT
Unclassified-Unlimited
Subject Category 23
Availability: NASA CASI (443) 757-5802

13. SUPPLEMENTARY NOTES
An electronic version can be found at http://ntrs.nasa.gov.

14. ABSTRACT

We present results of a molecular dynamic analysis of welding at the polymer-polymer interface. The analysis is performed for polyetherimide/polycarbonate polymer blends. The work is motivated by the applications to 3D manufacturing in space. In the first part of the report, we discuss bulk and spectral characteristics of the amorphous polymer blends. The vibrational and infra-red spectra obtained using auto-correlation functions calculations in molecular dynamics are compared with the experimental spectra. The mechanical and thermal properties of the samples including heat capacity, bulk modulus, and thermal expansion coefficients are estimated and compared with experimental values. In the second part of the report, we discuss the result of molecular dynamical modeling of shear viscosity in a fully atomistic model of amorphous polymer blends with flat interface. The key result of the research is the demonstration of shear thinning behavior of the shear viscosity as a function of shear rate which is in good agreement with experimental data.

15. SUBJECT TERMS
polymer, additive manufacturing, interface, welding, molecular dynamics

16. SECURITY CLASSIFICATION OF:			17. LIMITATION OF ABSTRACT	18. NUMBER OF PAGES	19a. NAME OF RESPONSIBLE PERSON
a. REPORT	b. ABSTRACT	c. THIS PAGE			STI Help Desk (email: help@sti.nasa.gov)
U	U	U	UU	78	19b. TELEPHONE NUMBER *(Include area code)* (443) 757-5802